Global atmospheric inversion of the anthropogenic NH_3 emissions over 2019-2022 using the LMDZ-INCA chemistry-transport model and the IASI NH_3 observations

Pramod Kumar[1], Grégoire Broquet[1], Didier Hauglustaine[1], Maureen Beaudor[1,7], Lieven Clarisse[2], Martin Van Damme[2,3], Pierre Coheur[2], Anne Cozic[1], Bo Zheng[4], Beatriz Revilla Romero[5], Antony Delavois[6], Philippe Ciais[1]

[1]Laboratoire des Sciences du Climat et de l'Environnement (LSCE/IPSL), CEA-CNRS-UVSQ, Université Paris-Saclay, Gif-sur-Yvette, France
[2]Spectroscopy, Quantum Chemistry and Atmospheric Remote Sensing, Université libre de Bruxelles (ULB), Brussels, Belgium
[3]Royal Belgian Institute for Space Aeronomy, Brussels, Belgium
[4]Institute of Environment and Ecology, Tsinghua Shenzhen International Graduate School, Tsinghua University, Shenzhen, China
[5]GMV, Remote Sensing & Geospatial Analytics Division, Spain
[6]European Space Agency, ESRIN, Via Galileo Galilei, Frascati, Italy
[7]Currently at: High Meadows Environmental Institute, Princeton University, NJ, 08540, USA

Correspondence to: Pramod Kumar (pramod.kumar@lsce.ipsl.fr)

Abstract.

Ammonia (NH_3) emissions have been on continuous rise due to extensive fertilizer usage in agriculture and increasing production of manure and livestock. However, the current global to national NH_3 emission inventories exhibit large uncertainties ~~at all the spatiotemporal scales~~. We provide atmospheric inversion estimates of the global NH_3 emissions over 2019-2022 at 1.27°×2.5° horizontal and daily (at 10-day scale) resolution. We use IASI-ANNI-NH3-v4 satellite observations, simulations of NH_3 concentrations with chemistry-transport model LMDZ-INCA, and finite difference mass-balance approach for inversions of global NH_3 emissions. We take advantage of the averaging kernels provided in IASI-ANNI-NH3-v4 dataset, by applying them consistently to LMDZ-INCA NH_3 simulations for comparison to the observations and then to invert emissions. The average global anthropogenic NH_3 emissions over 2019-2022 is estimated as ~97~~8~~ (94~~5~~-100~~1~~) Tg yr^{-1}, which is ~613~~3~~% (~557~~7~~%-658~~8~~%) higher than the prior CEDS inventory's anthropogenic NH_3 emissions and significantly higher than two other global inventories: CAMS's anthropogenic NH_3 emissions (by a factor of ~1.8~~9~~) and CAMEO's agricultural and natural soil NH_3 emissions (by ~1.4 times). The global and regional budgets are mostly within the range of other inversion estimates. The analysis provides confidence in their seasonal variability and continental to regional scale budgets. Our analysis shows rise in NH_3 emissions by ~54% to ~373% during COVID-19 lockdowns in 2020 over different regions compared to the same-period emissions in 2019. However, this rise is probably due to a decrease in atmospheric NH3 sinks due to decline in NOx and SO_2 emissions during the lockdowns.

1 Introduction

Ammonia (NH_3) plays a critical role in both atmospheric chemistry and ecosystem's nitrogen and carbon cycling, with significant implications for air quality and human health, climate change, and agriculture. Ammonia in the Earth's atmosphere originates from both natural and anthropogenic sources, with the latter dominating emissions from the former. The agricultural sector is the largest source of NH_3 emissions contributing to more than 81% of the total global NH_3 emissions (Van Damme et al., 2021; Wyer et al., 2022) and other anthropogenic sources of NH_3 mainly stem from domestic, vehicular, waste water treatment, and industrial activities (Behera et al., 2013a; Sutton et al., 2013). Global future NH_3 emissions in 2100 are projected to increase by 30% to 50% compared to present-day levels, depending on the different Shared Socio-economic Pathways scenarios (Beaudor et al., 2024). Precise information on the NH_3 sources and quantitative attribution of emissions to these sources and atmospheric NH_3 concentration observations is essential in evaluating the impacts of NH_3 on ecosystems, climate,

air quality, and human health, and formulating effective mitigation measures (Zhu et al., 2015). Timely estimates of global anthropogenic NH_3 emissions are needed to formulate effective control strategies to reduce such emissions activities (Behera et al., 2013).

Bottom-up NH_3 emission inventories provide data on NH_3 sources and their emissions (Beaudor et al., 2023; Bouwman et al., 1997; Vira et al., 2020), enabling their integration into atmospheric chemistry-transport, climate models to simulate atmospheric ammonia concentrations, and assessing impacts of NH_3 emissions. However, significant uncertainties are inherent in bottom-up NH_3 emission inventories across spatiotemporal scales (Behera et al., 2013a; Luo et al., 2022; Sutton et al., 2013), stemming from the constraints of limited NH_3 emission activity data and emission factors, high uncertainty of agriculture statistics, and a lack of recent information (Chen et al., 2021; Crippa et al., 2018; Xu et al., 2019). In situ measurements are essential for accurately developing NH_3 emission inventories and for inversion of NH_3 emissions, as well as for evaluating these emissions. However, the scarcity of in-situ NH_3 measurements worldwide contributed to significant uncertainties in NH_3 emissions and in our understanding of NH_3 sources and their distributions (Zhu et al., 2015). Advancements in satellite measurements of columnar NH_3 abundance in the atmosphere in the past decades, provide high spatiotemporal resolution column concentration data, and inversion methods are progressively enhancing our ability to derive NH_3 emissions. For the atmospheric inverse modeling of the NH_3 emissions, satellite observations offer valuable data density and coverage, thus mitigating some of the limitations of the use of in-situ NH_3 measurements, enabling a more comprehensive assessment of NH_3 emissions. The recent NH_3 emission estimates based on satellite observations exhibit significant differences at both regional and global scales when compared to those reported by the bottom-up inventories (Cao et al., 2020; Chen et al., 2021; Van Damme et al., 2018; Luo et al., 2022; Evangeliou et al., 2021; Dammers et al., 2022). However, the satellite data also have some limitations, often lacking clear signals from the emissions outside the strongly polluted regions, bearing potential errors due to interference from other atmospheric constituents and to the complexity of their validation and calibration, and being sensitive to cloud cover and, in particular, providing an incomplete coverage in certain regions in presence of clouds.

Currently, satellite NH_3 observations are available from instruments such as: the Atmospheric Infrared Sounder (AIRS) on the NASA EOS Aqua satellite (Warner et al., 2016), the Aura Tropospheric Emission Spectrometer (TES) onboard EOS Aura satellite (Beer et al., 2008), the three of the Infrared Atmospheric Sounding Interferometer (IASI) series of instruments on the MetOp (Meteorological Operational satellite programme) satellites (Clarisse et al., 2009; Van Damme et al., 2021), the Thermal and Near-infrared Spectrometer for Observation-Fourier Transform Spectrometer (TANSO-FTS) onboard the Greenhouse Gases Observing Satellite (GOSAT) (Someya et al., 2020), and three Cross-Track Infrared Sounder (CrIS) instruments onboard the Suomi National Polar-orbiting Partnership (Suomi-NPP) satellites (Shephard et al., 2020). These datasets vary in their data record lengths, spatial coverage, and retrieval approaches. ~~However, most of the satellite data constrained NH_3 emission estimates are based on~~ The NH_3 observations derived from the IASI and CrIS measurements, which have similar instrumental characteristics but employ different retrieval approaches, are the most commonly used satellite data for constraining NH_3 emission estimates. The IASI NH_3 product is a widely used dataset as it provides continuous, long-term sampling commencing from 2007, with twice daily coverage across the globe. Except for its first version, subsequent versions of the IASI NH_3 data products are based on the Artificial Neural Network for IASI (ANNI) approach for retrieval of NH_3 total columns (Van Damme et al., 2017, 2021; Whitburn et al., 2016). However, the absence of the vertical averaging kernel (AK) in the IASI ANNI NH_3 previous products hindered their utility for comprehensive comparisons to atmospheric chemistry-transport model and its suitability for assimilation in atmospheric inversion processes for NH_3 emission estimations. The AK is proportional to the measurement vertical sensitivity profile and also describes the vertical structure of the impact of a priori information on the retrieval of NH_3 columns. When comparing a chemistry transport model against the satellite column retrievals, e.g., in satellite data assimilation processes, the application of the ~~averaging kernel~~AK should remove the influence of errors resulting from the a priori (or an assumed) atmospheric NH_3 vertical profile used in the retrievals in the model-satellite

comparison (Eskes and Boersma, 2003). Using synthetic satellite column observations of another short-lived species NO_2, Cooper et al. (2020) examined the impact of differences between the modelled and a priori atmospheric vertical NO_2 profiles on inversion of NOx emission estimates and found that discrepancies led to up to 30% increase in root mean square errors for realistic conditions over polluted regions, with inverted emission errors rising as the difference between simulated and a priori profiles increases. The application of ~~averaging kernel~~AK enables the model-retrieval comparison to be independent of the a priori profile (Cooper et al., 2020; Douros et al., 2023). Recently, Clarisse et al. (2023) presented a new version 4 of ANNI retrieval framework including, for the first time, vertical AK in the IASI NH_3 data product. In this study, we use this new version 4 of IASI ANNI NH_3 dataset for comparison to the global chemistry-transport model simulations and for the atmospheric inversion of the global NH_3 emissions.

In recent years, numerous studies used satellite observations, mostly IASI and CrIS, to estimate NH_3 emissions over specific regions (Cao et al., 2020, 2022; Chen et al., 2021; Ding et al., 2024; Fortems-Cheiney et al., 2020; Tichý et al., 2023; Xia et al., 2025) or across the globe (Dammers et al., 2022; Evangeliou et al., 2021; Luo et al., 2022). Some recent regional scale inversion studies over the USA (Cao et al., 2020; Chen et al., 2021), China (Jin et al., 2023; Momeni et al., 2023), UK (Marais et al., 2021), and Europe (Cao et al., 2022; Ding et al., 2024; Van Der Graaf et al., 2022) show approximately 20%-100% differences between the inversion-based and the bottom-up NH_3 emissions. The NH_3 inversion problem raises challenges and requires a high spatial resolution of the emissions since the NH_3 emissions are highly localized due to short lifetime of a few hours to a day of ammonia in the atmosphere. The impact of the atmospheric chemistry challenges the linearization underlying the traditional inversion approaches or the use of relatively simple models of the atmospheric chemistry and transport. The conventional variational or Kalman filter approaches, which are among the most sophisticated ones, have been used for regional scale inversions (Cao et al., 2020, 2022; Ding et al., 2024; Jin et al., 2023). However, covering the globe at a suitable spatial resolution represents an inversion problem whose dimension makes the application of such approaches very demanding in terms of computational cost. That is probably why, compared to regional studies, global inversions of NH_3 emissions based on satellite observations are relatively scarce (Van Damme et al., 2018; Dammers et al., 2022; Evangeliou et al., 2021; Luo et al., 2022). Studies such as Van Damme et al. (2018) and Dammers et al. (2019), covered emissions worldwide, but focusing on the detection and estimation of NH_3 large point sources or hotspot areas. Using high-resolution maps of atmospheric ammonia from IASI, Van Damme et al. (2018) detected 248 NH_3 hotspot locations and large source regions across the globe and reported that the satellite data constrained NH_3 emissions for the source regions vary within a factor of three from the corresponding estimates extracted from the Emissions Database for Global Atmospheric Research (EDGAR) emission inventory. However, the emissions from these detected large NH_3 point sources or source regions only account for a small fraction of the overall global NH_3 emissions budget (Dammers et al., 2019). For instance, the cumulative NH_3 emissions from the 249 point sources identified by Dammers et al. (2019) contributed to merely 5% of the total global NH_3 emissions in the Hemispheric Transport Atmospheric Pollution version 2 (HTAPv2) inventory.

Only a very few global scale inversion studies provided more comprehensive timeseries of full NH_3 emission maps using computationally intensive inversion frameworks. Recently, Dammers et al. (2022) derived global NH_3 emission maps at a high spatial resolution (0.2°×0.2°) based on a multi-source gaussian plume method using CrIS observations, and discarding any chemistry or aerosols mechanism associated with the short-lived species NH_3 in the multi-source Gaussian plume method. They showed that satellite-based total NH_3 emissions over the globe are ~1.8 times higher than those reported in previously identified anthropogenic NH_3 source locations in CAMS-GLOB-ANT v4.2 global anthropogenic NH_3 emission inventory, and the total estimates rise to ~4 times greater when newly detected anthropogenic and natural sources are taken into account. However, this approach also introduces uncertainties in the estimates due to the assumption of a globally constant atmospheric lifetime for NH_3 which is a limiting factor on the basis that chemical loss and deposition are highly variable processes that can

change the lifetime drastically (Van Damme et al., 2018), and uncertainties in plume-spread, wind speed, and wind direction when fitting a multi-source Gaussian plume model to the observations.

In two recent studies of global inversion of NH_3 emissions using previous versions of IASI ANNI NH_3 data products, Evangeliou et al. (2021) and Luo et al. (2022) estimated long-term monthly global NH_3 emissions over a decade period starting from 2008 and reported their estimates to be higher than those in the bottom-up inventories. However, significance differences were observed between these two NH_3 emission estimates. In both studies, inversions rely on the NH_3 lifetime diagnosed differently from the simulations of different global chemistry-transport models (CTM), and the modelled NH_3 total columns. Evangeliou et al. (2021) applied a basic mass-balance inversion approach to estimate monthly NH_3 emissions in each grid cells as a ratio of the observed total NH_3 column from IASI and the lifetime of NH_3 computed from a CTM simulations. Using a previous version of IASI NH_3 observations, Luo et al. (2022) modified the basic mass-balance approach used in Evangeliou et al. (2021) by updating the prior NH_3 emissions with an additive correction term. This correction is proportional to the difference between the observed and modelled NH_3 columns and inversely proportional to the NH_3 lifetime estimated by accounting for the deposition fluxes of the whole NH_x (NH_3 + NH_4^+) family instead of only using the NH_3 losses. However, estimating lifetime of NH_3 in the atmosphere is more complex due to the impact of transport mechanisms, loss of atmospheric NH_3 by the formation of ammonium sulfate or ammonium nitrate particles (Cao et al., 2020), and nonlinearities in NH_3-related chemistry affecting deposition and concentration. Changes in NH_3 concentrations due to emission affect its lifetime through its interaction with the other trace chemical species like SO_2, NOx, HCl, HONO (Behera et al., 2013b) and the basic mass-balance approaches in Evangeliou et al. (2021) and Luo et al. (2022) do not consider the impact of NH_3 emission changes in their estimation of NH_3 lifetime in atmospheric inversions, which may affect the accuracy of emission estimates.

Variations of the mass-balance inversion methodology, such as, the finite difference mass-balance (FDMB) approach (Cooper et al., 2017; Lamsal et al., 2011), have been proposed for atmospheric inversion of emissions of short-lived species, which aims to reduce errors in basic mass-balance methods due to nonlinear sensitivity associated between a species emissions and ambient concentrations. The FDMB inversion approach is computationally efficient for the global scale inversions at coarse resolutions and it has been widely used for estimating anthropogenic surface emissions of short-lived species like NOx and SO_2 at global and regional scales (Cooper et al., 2017; Lamsal et al., 2011). It derives the fluxes by scaling a prior emission estimates, usually derived from bottom-up inventories. This scaling is derived from the computation of the local sensitivity of concentrations to local emission changes from simulations with a CTM, and from the relative differences between observations and the modelled columns. Only a few studies have investigated the FDMB approach for NH_3 emission inversion at regional scales: Momeni et al. (2023) and Li et al. (2019). They applied iterative FDMB approach to constrain the NH_3 emissions of East Asia with CrIS and North America with IASI satellite observations. In this study, we investigate the use of the FDMB approach at the global scale to derive maps of the NH_3 emissions at a relatively high temporal resolution worldwide. While earlier global-scale inversion studies by Luo et al. (2022) and Evangeliou et al. (2021) derived NH_3 emission estimates at the one-month scale, we aim to provide daily estimates at 10-day scale (deriving 10-day running average). The FDMB inversion approach involves a chemistry transport model for simulations of NH_3 concentrations. We use a global chemistry-aerosols transport model LMDZ-INCA (Hauglustaine et al., 2004, 2014) for global NH_3 concentration simulations. Our LMDZ-INCA model configuration has a relatively high spatial resolution of 1.27°×2.5° (latitude × longitude) horizontally, and 79 vertical levels. The absence of the averaging kernel in previous versions of IASI ANNI NH_3 data products used in the previous inversion studies prevented utilization of this information to integrate the modelled NH_3 profile consistently with the IASI NH_3 retrievals. This limitation may have impacted the final NH_3 emission estimates. In this study, we take advantage of the availability of AKs in version 4 of IASI NH_3 product for suitable assimilation of such data into a global inversion framework relying on a CTM. The application of AK in our global atmospheric inversion of NH_3 emissions with the new version 4 of the IASI NH_3 retrievals is one of the main features in this study.

Here, we estimate global daily (as a 10-day running average) anthropogenic NH_3 emissions over the land at 1.27°×2.5° horizontal resolution across a period of four years from 2019 to 2022 using the new version 4 of IASI ANNI NH_3 data product and the FDMB inversion approach (Cooper et al., 2017; Lamsal et al., 2011). We first compare the LMDZ-INCA model global NH_3 simulations against the IASI NH_3 observations to assess our model's performance and its suitability for global inversions of NH_3 emissions. In both model-satellite comparisons and inversions, we take advantage of averaging kernels provided in the version 4 of IASI ANNI NH_3 data product to remove the impact of the vertical NH_3 profile assumption in~~of~~ the retrievals. We present and discuss the results of our model comparison analysis with the IASI NH_3 observations and the global inversions of the NH_3 emissions at both global and regional scales, considering temporal scales ranging from daily (10-day scale) to monthly, seasonal, and annual. We evaluated our inversion approach and emissions estimates by conducting LMDZ-INCA simulations using the optimized NH_3 emissions and comparing the model results with the IASI NH_3 observations. Finally, we compare our estimated global NH_3 emissions with independent global bottom-up inventories and other estimated NH_3 emissions over the globe and over the selected regions. The structure of the paper is as follows. Section 2 describes the new version 4 of the IASI NH_3 observations, chemistry-transport model and its setup for global NH_3 concentration simulations, our strategy to compare model NH_3 simulations with the satellite observations, and the FDMB inversion approach used for global daily NH_3 emission estimations. Section 3 presents the results followed by their discussions and limitations of the study in section 4. Key conclusions of this study are provided in section 5.

2 Material and methods

2.1 IASI NH_3 version 4 observations

IASI is an infrared Fourier transform spectrometer onboard the Sun-synchronous polar-orbiting Metop-A/B/C satellites, which were respectively launched in 2006, 2012, and 2018 (Clerbaux et al., 2009). IASI has a cross-track scanning swath width of ~2200 km, with a pixel size of ~12 km in diameter at nadir. Each instrument onboard one of the sun-synchronous satellites covers almost all locations over the globe twice a day, once at daytime and once at nighttime, with overpasses around 09:30 and 21:30 local solar time (LST), respectively. The vertical sensitivity of the IASI NH_3 measurements, mainly in the boundary layer where NH_3 is predominantly confined, varies as a function of the thermal contrast between the surface and the atmospheric layers (Clarisse et al., 2010; Di Gioacchino et al., 2024). The NH_3 total column observations from the IASI measurements in the first version were retrieved using the so-called hyperspectral range index (HRI) in an extended spectral range (800-1200 cm^{-1}) and using look-up-tables (LUT) built from forward radiative transfer model simulations (Van Damme et al., 2014). In the subsequent versions, an Artificial Neural Network for IASI (ANNI) retrieval approach was then developed and used for retrievals of IASI NH_3 total columns (Van Damme et al., 2017, 2021; Whitburn et al., 2016). The ANNI NH_3 retrieval approach uses an assumed Gaussian-shaped vertical profile of NH_3 volume mixing ratio (the "prior" profile), which is modelled as a function of altitude above the ground or ocean surface ~~level~~, the peak concentration altitude, and the width of the profile of significant NH_3 concentrations. The peak altitude over land is set at the ground surface with a width equal to the boundary layer height (Clarisse et al., 2023), as the NH_3 emission is generally higher near the surface and NH_3-related chemistry and dispersion cause concentration to decrease with altitude. Whereas, over the ocean, it is set to 1.4 km with a width of 0.9 km (Clarisse et al., 2023). In this study, we use daily NH_3 total columns from a recently released version 4 (ANNI-NH3-v4) of the IASI ANNI retrievals of NH_3 (Clarisse et al., 2023). The most important feature of this new ANNI-NH3-v4 data product is the introduction of the column averaging kernel (AK). The vertical AK is essential for comparison of chemistry-transport model simulations against the satellite NH_3 retrievals, which can be used to remove the effect of the prior vertical NH_3 profiles used in the retrievals of the IASI NH_3 total columns in the model-satellite comparison. Note that the NH_3 distribution from IASI-ANNI-v4 is very similar to the ones with previous version 3, although values are about 15-20% larger due to the improved setup of HRI (Clarisse et al., 2023). Furthermore, the ANNI-NH3-v4 data product provides a more accurate

characterization of the measurement uncertainty, along with several other changes, resulting in the improved temporal consistency of the IASI NH_3 dataset spanning from 2007 ~~to 2023~~ onwards (Clarisse et al., 2023).

We use daily IASI-NH3-v4 NH_3 global observations over land from the Metop-B satellite from 2019 to 2022. We select the NH_3 observations from the morning overpass (around 09:30 ~~local solar time~~LST) only because of the better precision of morning observations as IASI is more sensitive at this time of day to the atmospheric boundary layer, where the signature of the surface emissions is the higher, owing to more favorable thermal conditions. We use high-quality IASI NH_3 observations only with the cloud coverage lower than and equal to 10% (Clarisse et al., 2023). We applied pre- and post-retrieval filters which accompany the dataset. The~~is~~ application of these filters removes respectively the observations corresponding to erroneous L1 processing of the spectra or excess cloud coverage, and observations corresponding to measurements with limited or no sensitivity to the measured quantity and retrievals satisfying certain threshold conditions (Clarisse et al., 2023).

2.2 LMDZ-INCA global chemistry-transport model and simulations

We use the global climate-aerosol-chemistry transport model LMDZ-INCA to simulate the global NH_3 concentrations, along with a state-of-the art gas phase tropospheric chemistry scheme as well as aerosols including sulfate, nitrate, black carbon (BC), particulate organic matter (POM), dust and sea-salt. LMDZ-INCA is a coupled model based on an atmospheric general circulation model (GCM) LMDZ V6 (Laboratoire de Météorologie Dynamique) (Boucher et al., 2020; Hourdin et al., 2020), a chemistry and aerosols model INCA V6 (INteraction with Chemistry and Aerosol) (Hauglustaine et al., 2004, 2014), and a global land surface dynamical vegetation model ORCHIDEE (ORganizing Carbon and Hydrology In Dynamic Ecosystems) (Krinner et al., 2005). The model uses a monotonic finite-volume second order parameterization to calculate large-scale advection of water vapor, liquid and solid water, and tracers (Boucher et al., 2020). The model uses the "New Physics" (NP) version of the physical parameterizations, which includes a turbulent scheme based on the prognostic equation for the turbulent kinetic energy (Yamada, 1983), the "Thermal Plume Model" for the convective boundary layer (Rio and Hourdin, 2008), a parameterization for cold pools and wakes resulting from convective rainfall evaporation (Grandpeix and Lafore, 2010), and Emanuel's deep convection parameterization scheme (Emanuel, 1991). LMDZ-INCA interactively accounts for the emissions, transport (resolved and subgrid scales), deposition (both dry and wet) of chemical species and aerosol, and incorporates a full chemical scheme for the NH_3 cycle and nitrate particle formation (Hauglustaine et al., 2014).

LMDZ-INCA model configuration used in this study has a horizontal resolution of 1.27° in latitude × 2.5° in longitude and with 79 hybrid σ-pressure levels within a terrain following vertical coordinate stretches up to 80 km. We conducted LMDZ-INCA spin-up simulations from 2010 to 2018 and then reference simulations for a period of four years from 2019 to 2022, which we use for the model comparison with the IASI NH_3 observations and for the global NH_3 emission inversions. The simulations were driven by nudging the GCM winds with a 3.6 h relaxation time to the 6-hourly ECMWF Reanalysis v5 (ERA5) data, regridded onto the LMDZ-INCA model grid. In LMDZ-INCA simulations, we used monthly global anthropogenic emission of the chemical species and gases, including NH_3, from the open-source Community Emissions Data System (CEDS) global bottom-up gridded inventories (McDuffie et al., 2020) with an initial horizontal resolution of 0.5°×0.5° and interpolated onto the model horizontal grid. We use conservative regridding by ensuring that the total mass (e.g., emissions) is preserved during the interpolation. The CEDS global emission inventories provides emissions of NH_3, NOx, SO_2, NMVOCs, CO, OC, and BC from eleven anthropogenic sectors, including agriculture, energy, on-road, non-road transportation, residential, commercial, waste solvents, international shipping, and others (McDuffie et al., 2020). ~~We also use~~ The CEDS inventory also includes emissions of NO and NH_3 from agricultural soils with both synthetic and manure fertilizers. Since CEDS anthropogenic emissions are available only up to 2019, the CEDS emission fluxes for the post-2019 years were developed based on the combination of the CEDS emissions in 2019 with the carbon emission growth rate from 2019 to the target year. The data on emissions growth rate are derived from the Carbon Monitor dataset (https://carbonmonitor.org/) and calculated by source sector, by month, and by country. This approach to extrapolate emission fluxes based on CO2 data has

been commonly applied to various species, particularly those associated with the fossil fuel emissions. The led to noticeable variations in emissions of species like SO_2 and NOx, which have been simultaneously used in the LMDZ-INCA simulations with full chemical scheme for sulfate and nitrate particles formation. However, as extrapolation calculations are conducted for each source sector separately and NH_3 emissions mostly come from agricultural activities, which do not emit CO_2 directly, applying this approach to extrapolate NH_3 emissions for the post-2019 years resulted in almost invariant NH_3 emissions after 2019. While this approach may seem simplistic for NH_3 fluxes, it is used in this study to construct the spatial distribution of prior emissions, as we expect satellite data to drive year-to-year variations in the final inversion results. Since the anthropogenic emissions are derived from the CEDS inventory at a monthly resolution, they are uniformly distributed in time at the hourly resolution in the input to the LMDZ-INCA simulations, without incorporating diurnal cycles. We use fire emissions from the Global Fire Emissions Database (GFED4) (Van Der Werf et al., 2017), and biogenic volatile organic compound (VOC) emissions calculated from the ORCHIDEE vegetation model (Messina et al., 2016). Emission fluxes from anthropogenic and natural sources are prescribed to the model as monthly forcing files for different species. We sample the simulated NH_3 concentration at an hourly frequency over a four years period from 2019 to 2022. We use these hourly LMDZ-INCA model simulated NH_3 dataset for our analysis and inversions with IASI NH_3 observations from the morning overpass.

2.3 Model and satellite comparison approach

The retrievals of NH_3 total columns observations, Ω_{obs}, where "*obs*" stands for "*observed*" IASI NH_3 total columns in the IASI ANNI-NH3-v4 data product, are implicitly dependent on an assumed (prior) Gaussian-shaped vertical profiles of the NH_3 volume mixing ratio above the land and sea surfaces (Clarisse et al., 2023). As a result, the comparison between satellite-retrieved and model-simulated column abundances is influenced by the shape of the vertical profile of NH_3 mixing ratios assumed in the retrievals. The total column averaging kernel (AK), as provided in the ANNI-NH3-v4 data product, characterizes the altitude-dependent sensitivity of the retrieved atmospheric column to changes in true profile (Eskes and Boersma, 2003). The importance of the AK in correctly comparing model simulations with the satellite observations has long been established ~~f~~(Cooper et al., 2020; Douros et al., 2023 for NOx; Koukouli et al., 2018 for SO2). There are several possible approaches of comparing model simulations with the satellite observations enabling the model-retrieval comparison to be independent of assumption on the profiles in the retrievals (Cooper et al., 2020; Douros et al., 2023; Cao et al., 2022; Ding et al., 2024). Here, we convolved the simulated LMDZ-INCA NH_3 vertical profiles with the IASI NH_3 total column ~~averaging kernels~~AKs. The convolved LMDZ-INCA model simulation of the NH_3 columns, Ω_{mod}, where "*mod*" stands for "*modelled*" LMDZ-INCA NH_3 total column, is obtained by weighting the vertical integration of the model NH_3 sub-columns (x_l) with the averaging kernel (AK_l) (Clarisse et al., 2023; Eskes and Boersma, 2003):

$$\Omega_{mod} = \sum_l AK_l \, x_l \qquad (1)$$

where the summation over l is over the 14 vertical levels of IASI NH_3 retrievals (on which an assumed NH_3 vertical profile and AKs of retrievals are defined). Here, x_l are obtained by interpolating LMDZ-INCA original NH_3 mole fraction vertical profiles (at 79 levels) onto the levels corresponding to IASI ANNI-NH3-v4 retrievals (14 levels). The interpolation is performed in a manner that conserves the NH_3 total column amount. The application of the ~~averaging kernel~~AK to the simulated LMDZ-INCA NH_3 profile ensures the elimination of an assumed NH_3 profile error contribution to model-satellite comparison (Boersma et al., 2004; Eskes and Boersma, 2003), and that the model simulated column is integrated in a way that reflects the retrieval sensitivity.

In order to illustrate the impact of the ~~averaging kernel~~AK on modelled NH_3 total columns, Figure 1 shows LMDZ-INCA simulated NH_3 mole fraction vertical profiles over a model grid cell in India on three clear-sky days (February 24, March 30, October 28) in 2019, and the modelled NH_3 sub-columns with and without the application of the ~~averaging kernel~~AKs corresponding to one of the IASI pixel in that model grid cell, obtained from the modelled NH_3 mole fraction profile interpolated on the vertical levels of IASI ANNNI-NH3-v4 retrievals. Despite the AK values varying relatively smoothly with

altitude above the ground surface, the application of the AK can amplify modeled NH_3 sub-columns at higher altitudes compared to those calculated without the AK (Figure 1). This effect is generally due to the interaction between the vertical structure of the modeled NH_3 vertical profile and the thickness (or pressure width) of the sub-columns. Since each NH_3 sub-column represents the mass of NH_3 within a specific pressure layer, layers with both significant NH_3 concentrations and wider pressure intervals can result in larger NH_3 sub-column values, even if the AK is not at its peak for those layers (Figure 1). Consequently, even modest AK values at higher altitudes, combined with substantial NH_3 mass in thick pressure layers, can lead to amplified contributions to the total column. The subfigures in Figure 1 show that the LMDZ-INCA NH_3 local vertical profiles mostly decrease with the altitude and are almost similar the Gaussian-shaped NH_3 vertical profile centered at the land surface used as a prior in the IASI ANNI-NH3-v4 retrievals. However, the model simulated vertical NH_3 profiles for some days (e.g., Figure 1(b)) deviate from such a general smoothed NH_3 vertical profile shape assumed in the IASI NH_3 retrievals and show secondary peak(s) at some higher altitude. Although the short-lived species like NH_3 largely resides within the atmospheric boundary layer and the long-term averaged NH_3 vertical distribution in the boundary layer or in the lower troposphere could be assumed as smoothly decreasing with the altitudes with maximum at the land surface, high-temporal-scale NH_3 vertical profiles corresponding to the IASI overpass time can be a little more complex than this averaged smoothed profile, as observed in both model simulations (Figure 1(b)) and aircraft- and surface-based in-situ measurements (Cady-Pereira et al., 2024; Guo et al., 2021; Pu et al., 2020). This suggests a potential need to refine the assumed NH_3 vertical profile for more accurate satellite NH_3 retrievals, though the necessity for this refinement may depend on specific locations and meteorological conditions. Across all these days, the application of the ~~averaging kernel~~AK results in higher LMDZ-INCA NH_3 total column values compared to the ones without applying the AKs. The ~~averaging kernel~~AK from ANNI-NH3-v4 product, often exhibits magnitudes exceeding unity at altitudes corresponding to the LMDZ-INCA NH_3 sub-columns peak altitudes. This results in larger modelled NH_3 total column values when using the ~~averaging kernel~~AK.

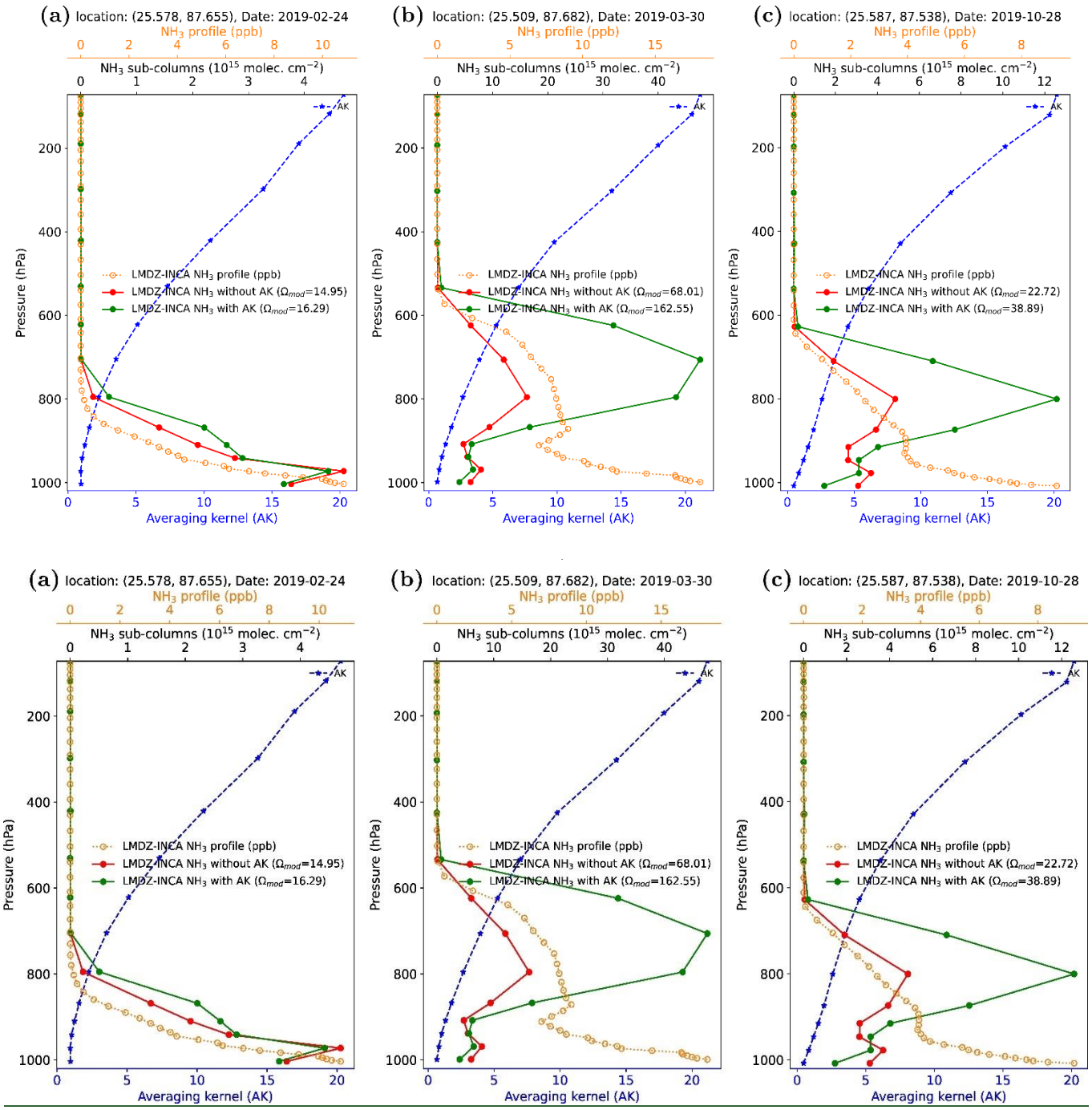

Figure 1: An example illustrating the convolution of LMDZ-INCA NH_3 vertical profiles with the IASI ANNI-NH3-v4 averaging kernel (AK) to calculate the convolved LMDZ-INCA modelled NH_3 total column (Ω_{mod}). The LMDZ-INCA original NH_3 mole fraction vertical profile (in ppb) at 79 model levels (represented by the orange dashed line on the secondary x-axis on top) and the ~~averaging kernel~~ AK from individual IASI NH_3 pixels (represented by the blue dashed line on the primary x-axis on bottom) within a model grid cell centered at (25.5, 87.6) in India on three dates: (a) 24 February 2019, (b) 30 March 2019, and (c) 28 October 2019, and the corresponding NH_3 sub-columns (in molecules cm^{-2}) (secondary x-axis on top) from the NH_3 vertical profiles simulated by LMDZ-INCA in this grid-cell interpolated on the vertical levels of assumed NH_3 profile in IASI retrievals (shown in red), and the convolved LMDZ-INCA sub-column profiles with the ~~averaging kernel~~AK (displayed in green). The values of ~~the LMDZ-INCA NH_3 total column (Ω_{mod})~~ with and without using the AK (in molecules cm^{-2}) are also presented on the respective sub-plots for each day.

At a given hourly output of the model simulations with the IASI observations from morning overpass around 09:30 LST, we derive a corresponding LMDZ-INCA NH_3 profile for each individual IASI NH_3 pixel within a model grid cell that contains the center of this pixel, and derive the convolved LMDZ-INCA modelled NH_3 total column by applying the corresponding AK. Since IASI resolution is much finer than that of LMDZ-INCA, this process yields several convolved modeled NH_3 total columns for a single model grid cell. We then average these resulting observed (Ω_{obs}) and corresponding AK-convolved

modelled NH_3 total columns (Ω_{mod}) at the model spatial resolution (1.27° × 2.5°) for a proper comparison at the coarsest resolution between the two products. We exclude the grids of the averaged NH_3 total columns from the analysis if there are fewer than four high-quality IASI pixels within a model spatial grid or if the grid-cell average of observations is negative due to some negative IASI NH_3 total column retrievals.

2.4 Inversion of the global NH_3 emission from IASI observations

We use the finite difference mass-balance (FDMB) inversion approach (Cooper et al., 2017; Lamsal et al., 2011) for the global inversion of NH_3 emissions using NH_3 total columns from LMDZ-INCA model simulations and IASI NH_3 observations. The inversion approach assumes that the short lifetime of NH_3 of a few hours to a day in the atmosphere, limits its horizontal transport on coarse grids, and implicitly conducts local analysis, deriving local surface emissions (in a given model horizontal grid cell) based on local observations (corresponding the same model horizontal grid cell), even though relying on full 4D (3D in space, 1D in time) simulations with LMDZ-INCA. The FDMB inversion approach relies on the estimation of the local sensitivities (β) of the simulations of NH_3 total columns to change in the local NH_3 emission, addressing non-linear chemistry affects from the model simulations. It derives NH_3 emission estimates at each grid cell by scaling a prior NH_3 emission (here based on the anthropogenic emissions from the CEDS inventory), considering the local sensitivity of NH_3 simulations to changes in emission and the relative difference between the observed and modelled NH_3 total columns. Our objective is a daily estimate of 10-day running mean global anthropogenic NH_3 emissions over land. However, with only satellite NH_3 observations, it is challenging to distinguish between anthropogenic and natural sources. Therefore, our approach focuses solely on grid-cells and days where and when the prior NH_3 emission inventory indicates that the emissions are dominated by the anthropogenic sources, and where and when we have retained grid-cell averages of IASI NH_3 observations (see section 2.3). We use the daily- combined anthropogenic NH_3 emissions from CEDS and fire emissions from the GFED4 inventories, which are derived from monthly data and uniformly distributed at the hourly scale within each day ~~used~~ in the LMDZ-INCA simulations, as a priori emissions (E_a) in the inversions. We select the grid cells with dominating anthropogenic NH_3 emissions by identifying those where a ratio of anthropogenic NH_3 emissions to total NH_3 emissions (including anthropogenic, biogenic and fire NH_3 emissions) is greater than 0.6. This selection of dominant anthropogenic emissions slightly alters their spatial distribution over the years from 2019 onward due to variations in fire emissions across different years. We compute a 10-day running average at each grid cell of the modelled and observed NH_3 total columns and of the a priori emissions to smooth out the daily fluctuations in observed NH_3 total columns and to increase the sample size and spatial coverage of the daily flux estimates. Following ~~(~~Cooper et al., (2017) and~~;~~ Lamsal et al., (2011), for a given day and over each model horizontal grid-cell, the satellite-constrained NH_3 emission estimates (E_{IASI}) using the observed IASI NH_3 total columns (Ω_{obs}), and the modelled LMDZ-INCA columns convolved with the ~~averaging kernel~~AKs (Ω_{mod}) corresponding to a priori NH_3 emission (E_a) used in the model simulations are calculated as:

$$E_{\mathrm{IASI}} = E_a \left(1 + \beta \frac{\Omega_{obs} - \Omega_{mod}}{\Omega_{mod}}\right) \qquad (2)$$

where a unitless scaling factor β accounts for the local sensitivity of the modelled NH_3 total columns ($\Delta\Omega_{mod}/\Omega_{mod}$) to perturbations of the a priori NH_3 emissions ($\Delta E_a/E_a$), and is defined as:

$$\beta = \frac{\Delta E_a / \mathrm{E}_a}{\Delta\Omega_{mod}/\Omega_{mod}} \qquad (3)$$

We perform two LMDZ-INCA model simulations for each year: one using the prior emissions, with the anthropogenic NH_3 emissions from the CEDS bottom-up inventory for the year 2019 which updated for subsequent years based on the trend of previous years NH_3 emissions (see section 2.2), and another with a 40% reduction in the CEDS anthropogenic NH_3 emissions to derive β. We applied some filters on β, on the observed and/or the modelled NH_3 total columns, and/or on the bottom-up emissions to select the grids corresponding to the dominating anthropogenic emissions, and to avoid negative or extreme unrealistic estimates of the NH_3 emissions from the inversions. We select grids over land only for (i) $0 \leq \beta \leq 10$, (ii)

$\beta \frac{\Omega_{obs} - \Omega_{mod}}{\Omega_{mod}} \geq -1$, (iii) Ω_{mod} and $\Omega_{obs} > 1 \times 10^{15}$ molecules cm^{-2}. Figure S1 in supporting information shows an example of the distribution of monthly mean values of β for July 2019. The values of β are less than 1.5 over most of the major NH3 emitted land regions ~~over the globe~~worldwide ~~on land regions~~.

Satellite data gaps, and some filters applied on observations and different variables in the FDMB inversion approach to focus on model grid cells dominated by anthropogenic NH_3 emissions ~~(section 2.4)~~, result in numerous grids or days where NH_3 emissions could not be derived directly from the IASI NH_3 observations. Therefore, the derivation of national or regional budgets of anthropogenic emissions at daily (10-day scale) to monthly and annual scale from the satellite observations requires a proper gap-filling of grid cell or days for which the inversion protocol does not yield emission estimates. To fill these gaps in IASI-constrained NH_3 emissions, we use a rather conservative approach utilizing IASI-constrained NH_3 emissions and the corresponding a priori CEDS anthropogenic NH_3 emissions used in the inversions. The gap-filling is performed over some specific regions. In order to gap-fill the daily-unconstrained NH_3 emissions, we compute a daily scaling factor as a ratio between the IASI-constrained and the corresponding CEDS anthropogenic NH_3 emissions integrated over a specific region. The missing emissions in that selected region are gap-filled by multiplying in each corresponding grid-cell the CEDS NH_3 emissions with these scaling factors. For a given day, when the spatial coverage of the IASI-constrained anthropogenic NH_3 emissions is less than 60% in a specific region due to a poor satellite coverage and due to other data filtering to apply the FDMB inversion approach, we apply some constraints on the scaling factor to prevent spurious gap-filled emissions. If the IASI-constrained emissions coverage is less than 10%, we directly use the prior CEDS NH_3 emissions. For coverage between 10% and 40%, we cap the scaling factor at 1.25, and for coverage between 40% and 60%, we cap it at 1.5. For the gap-filling, we use ~~nine~~10 continental regions (illustrated in Figure S2~~4~~) ~~from the 10 regions~~over the main land worldwide defined by Ge et al. (2022) based on 58 IPCC reference regions representing consistent regional climate features described in Iturbide et al. (2020). Ge et al. (2022) used the~~se~~ nine regions (except the "rest of the world" region) ~~-~~to access global and regional budgets and fluxes of atmospheric reactive N and S gases and aerosols. The fraction of the IASI-constrained and the gap-filled NH_3 emissions per season across six regions for each year from 2019 to 2022 in Figure S3~~5~~ shows that the gap filling of emissions over most of the regions is mostly higher during winter season and minimum during spring. However, in some regions such as India and Africa, the percentage of the gap-filled emissions to the total seasonal emissions is higher in summer compared to other seasons due to relatively smaller numbers of satellite observations, caused by higher cloud coverage during the monsoon season. The overall percentage of the gap-filled NH_3 emissions to the total emissions over worldwide is maximum (up to ~2~~6~~8%) during winter and minimum (up to ~1~~0~~1%) during spring season and it ranges from ~15~~5~~6%-18~~8~~9% during summer and autumn (Figure S3~~5~~). However, since the attribution of the NH_3 emissions in winter season to the total annual emissions is smaller compared to other seasons, the total gap-filled emissions in winter are still lower than in other seasons (Figure S4~~6~~).

3 Results

We present the results from LMDZ-INCA model comparisons with satellite NH_3 observations and inversions of NH_3 emissions at both global and regional scales over land areas. For regional analysis, we select six major NH_3 source regions: India, China, Africa, Europe, North America, and South America (Figure S5~~2~~). We present and discuss our results across various temporal scales, ranging from daily to monthly, seasonal, and annual.

3.1 Model and satellite comparison of NH_3 total columns

We start by comparing the LMDZ-INCA model simulated NH_3 total columns driven by the prior emissions and convolved with the ~~averaging kernel~~AKs against the IASI NH_3 observations, with first a worldwide overview, and then some focuses on

regions over the land. In addition to assessing global and regional mean comparisons between the modeled and the observed IASI NH_3 columns, we also calculate the Pearson's correlation coefficient (r) and Root Mean Square Error (RMSE) between the annual or monthly mean simulated and observed values at the model grid level, as part of our comparative analysis (shown on Figures 2&3 for 2019 and Figures S6~~3~~ for all years from 2019 to 2022).

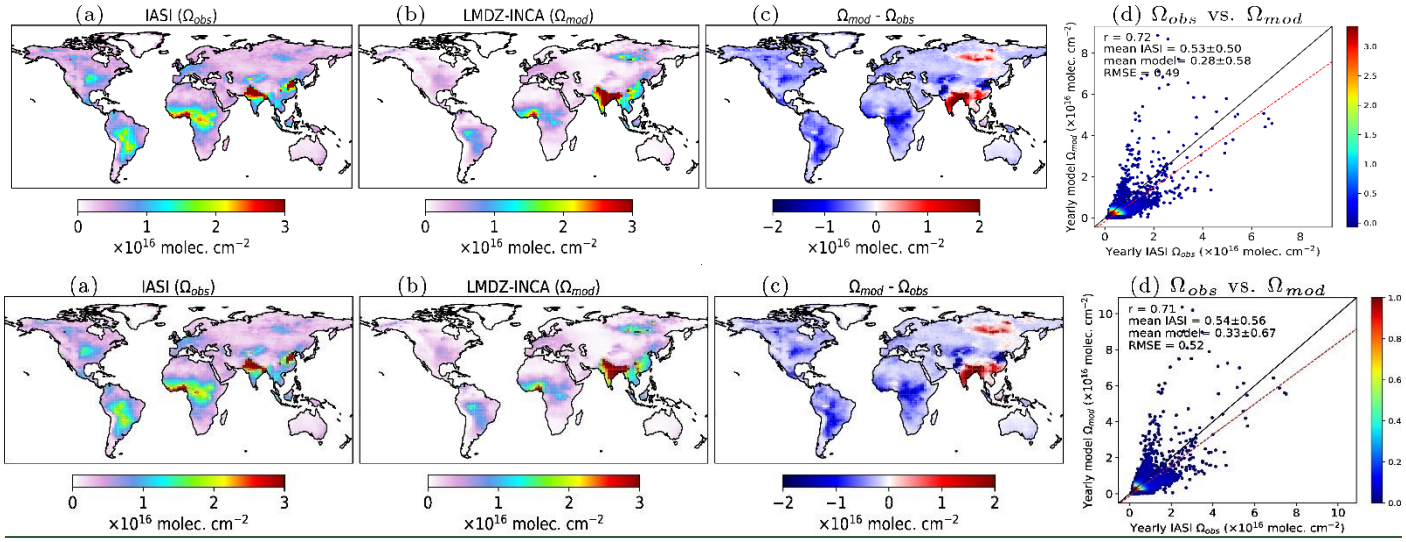

Figure ~~2~~2: The spatial distributions of the annual mean NH_3 total columns (in molecules cm^{-2}) for the year 2019 (a) from the IASI ANNI-NH3-v4 observations ($\boldsymbol{\Omega_{obs}}$), (b) from LMDZ-INCA model simulated columns after applying the averaging kernel ($\boldsymbol{\Omega_{mod}}$), and (c) the difference ($\boldsymbol{\Omega_{mod} - \Omega_{obs}}$) between them. The last column (d) show the scatter density plots between these annual means observed IASI and the corresponding LMDZ-INCA model NH_3 columns across all model grid-cells worldwide over the land. In the scatter plots, the solid black line represents the one-to-one line, while the dashed red line represents the regression line.

Figures 2 compares the annual mean modelled LMDZ-INCA NH_3 columns (Ω_{mod}) with the observed IASI NH_3 column retrievals (Ω_{obs}) re-gridded on the LMDZ-INCA model grid (1.27° × 2.5°) worldwide over land for the year 2019 (Figure S6~~3~~ for all four years from 2019 to 2022). It shows that the annual mean worldwide spatial distributions of the modelled NH_3 columns are approximately similar to that of the IASI NH_3 retrievals and there is a good spatial correlation (r = 0.~~72~~71) between them. However, the IASI NH_3 observations indicate higher NH_3 abundance compared to the LMDZ-INCA simulations across most of the regions worldwide, except over the south Asia and Eastern Siberia regions (Figure 1). We observe an overall underestimation of the global annual mean LMDZ-INCA NH_3 columns Ω_{mod} (mean: 0.~~28~~33×10^{16} molecules cm^{-2}) compared with the observed IASI retrievals Ω_{obs} (mean: 0.~~53~~54×10^{16} molecules cm^{-2}). The RMSE between the annual mean gridded Ω_{mod} and Ω_{obs} worldwide is 0.~~49~~52×10^{16} molecules cm^{-2}.

Emphasizing on the regional analysis, in Figure 3, we found that the modelled NH_3 total columns are lower than the IASI NH_3 observations over most of the selected regions, except over the Indian region (also south East Asia, not shown but see Figure 2), and also over a region in Eastern Siberia, where the model shows an overestimation of the observations (not shown but see Figures 2). The annual regional mean of monthly Ω_{mod} over China, Africa, Europe, South America, and North America regions are respectively ~~10~~4%, ~~51~~52%, ~~58~~53%, ~~60~~58%, and ~70~~2~~% smaller compared to Ω_{obs} (Figure 2). However, over the Indian region, the annual regional mean of Ω_{mod} is ~~41~~44% larger than Ω_{obs}. The monthly regional mean timeseries of the IASI NH_3 observations in Figure 3 show that the NH_3 columnar abundance over most of the regions are higher during spring and/or summer months compared to the winter. These elevated NH_3 columns observed during spring and/or summer months compared to winter months can be attributed to increased agricultural activities, particularly the prominent use of N-fertilizers in crops during warmer seasons. High NH_3 concentrations are also influenced by temperature, as warmer temperatures can enhance NH_3 volatilization from soils and agricultural surfaces (Sutton et al., 2013). This synergistic effect of agricultural practices and temperature contributes to the seasonal variation in NH_3 emissions, with higher concentrations during spring and/or summer months.

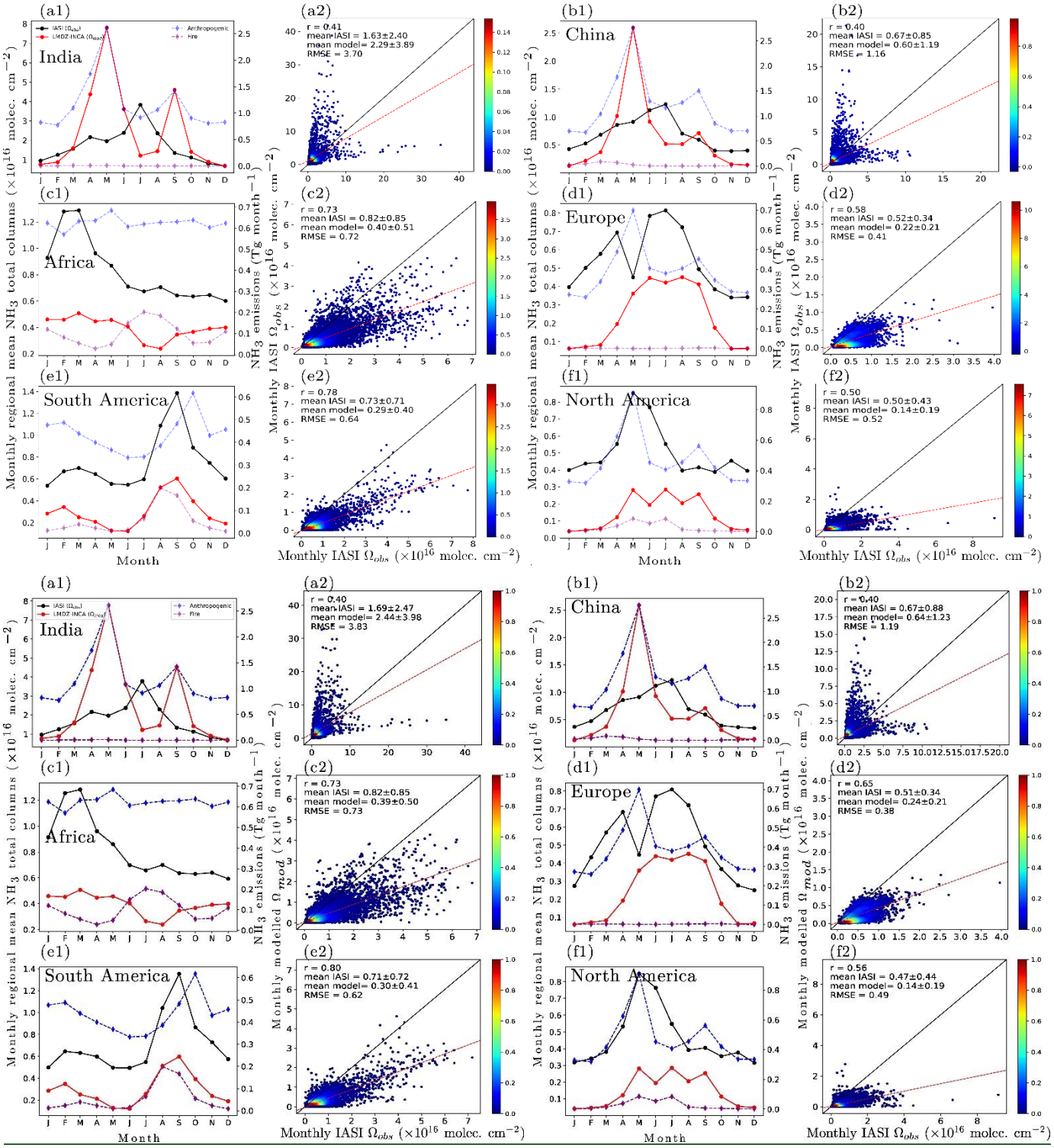

Figure 33: The monthly regional mean timeseries of the observed IASI NH_3 total columns ($\boldsymbol{\Omega_{obs}}$), the corresponding LMDZ-INCA modelled columns ($\boldsymbol{\Omega_{mod}}$) (primary y-axis), and monthly anthropogenic (CEDS) and fire (GFED4) NH_3 emissions (secondary y-axis) from bottom-up inventories used in the model simulations for the year 2019 for different selected regions (a) India, (b) China, (c) Africa, (d) Europe, (e) South America, and (f) North America (first column). The second column in each subfigure show the scatter density plots between the monthly mean gridded observed IASI and the corresponding modelled NH_3 total columns. In the scatter plot, the solid black lines represent the one-to-one line, while the dashed red lines represent the regression line.

The monthly mean modelled NH_3 columns in Figure 3 mostly follow the seasonal variation of the IASI observations over the South American and African regions, and over the European region up to some extent. However, for other remaining regions, especially over the Indian, Chinese, and the Middle East (not shown) regions, the seasonality of the modelled NH_3 columns largely deviates from the observations and we see a large scatter between the monthly mean gridded modelled and observed NH_3 columns (Figures 3-(a) and (b)). Over the Indian region, the model shows two main peaks with the highest peak in May

following a secondary smaller peak in September; whereas, the IASI observations show the highest peak in July and a smaller one in April (Figure 3(a1)). The high NH_3 loading from the IASI observations over the Indian region from June to August with a maximum peak in July and a secondary much smaller peak in April (Figure 3(a1)), is consistent with the cropping cycle (Kuttippurath et al., 2020), high usage of the N-fertilizers, and high temperature during these monsoon and summer months in the Indo-Gangetic Plain (IGP) region spanning the banks of the Indus and Ganges Rivers and their tributaries (Beale et al., 2022). However, as mentioned before, the variation and two distinct peaks in the modelled NH_3 columns is similar to the variation and peaks in the anthropogenic NH_3 emissions used in the model simulations (Figure 3). Similarly, over the Chinese region, the observed NH_3 columns show highest peak in July which is not captured by the simulations that shows the maximum peak in May, followed by a small peak in September. In these regions, because of differences of seasonal variations between the modelled and observed NH_3 columns, we see weak spatial correlations between the monthly mean observed and modelled gridded NH_3 columns (Figure 3) that are smaller than in other regions like Africa, South America, and Europe, where the seasonality in both modeled and observed NH_3 total columns is roughly similar.

Figure 3 also shows the seasonal cycles in the regional anthropogenic (CEDS) and fire (GFED4) emissions from the global emission inventories used in the model simulations. Over some regions like South America, North America, and Africa, fire NH_3 emission has visible contribution to this seasonal variation in total emissions; whereas, over India, China, and European regions, this attribution is very small (Figure 3). It shows that the seasonality in the modelled NH_3 total columns mostly varies with the seasonality in the combined anthropogenic and fire NH_3 emissions over these regions (Figure 3). Therefore, the seasonality differences between the model and observations over some regions are mostly due to different seasonality embedded in the prior NH_3 emissions used for the model simulations (Figure 3). The model comparison analysis for other years from 2020 to 2022 shows a similar behavior of the modelled and observed NH_3 columns. Notably, the seasonality of anthropogenic NH_3 emissions in the CEDS inventory is mainly derived according to the European agricultural practices based on the ECLIPSE v5 model, which leads to NH_3 emission peaks mostly in May and September corresponding to the fertilizers application before planting and after harvesting the crops (Beale et al., 2022). However, this seasonal variation of the NH_3 emissions in CEDS may not be accurately reflecting the diverse agricultural practices in other regions like India, China, and the Middle East (Figure 3) (Beale et al., 2022; Chen et al., 2023a; Kuttippurath et al., 2020). This is clearly evident from large difference in the seasonal variations between the IASI NH_3 observations and LMDZ-INCA model over these regions, as model is dominatingly driven by the CEDS anthropogenic NH_3 emissions in these regions (Figure 3). This dependency on European seasonality in CEDS inventory NH_3 emissions for other major agricultural NH_3 emission regions with diverse agricultural practices, like India and China, require for region-specific data to improve the accuracy of emission inventories. For some regions like the South America, Africa, and North America the observed IASI NH_3 total columns show high values during specific periods, which mainly attributes to heightened NH_3 loading resulting from biomass burning from wildfires in these regions. The underestimation and/or distinct seasonality of the modelled NH_3 columns compared to the observed IASI NH_3 retrievals over different regions indicate biases and/or differential seasonality in the prior NH_3 emissions from the inventories over these regions.

Previous validation studies of earlier IASI ANNI NH_3 retrieval products (e.g., with version 3) showed relatively good agreement with in situ and FTIR measurements (Guo et al., 2021; Wang et al., 2020). Although, the IASI-ANNI-NH3-v4 product introduces important improvements compared to the earlier versions and expects minimal biases, a comprehensive validation of this version has not yet been conducted and such a validation is anticipated in upcoming studies (Clarisse et al., 2023). Therefore, the bias between IASI NH_3 columns and LMDZ-INCA model simulations mainly reflect an underestimation of agricultural NH_3 emissions in the prior inventory, as well as a misrepresentation of their seasonal variation. However, we

cannot fully rule out remaining retrieval uncertainties in the absence of comprehensive validation of this version of the IASI NH_3 retrievals.

3.2 Evaluation of the estimated NH_3 emissions derived from inversions with the IASI NH_3 observations

In order to validate our atmospheric inversion approach (more specifically, to validate the linear approximation of the atmospheric chemistry model based on a single perturbed emission simulation) and strengthen our confidence in the NH_3 emission estimates, we have conducted a LMDZ-INCA model simulation using the IASI-constrained NH_3 emission estimates derived from our global inversions for the year 2019 and compared the simulated NH_3 total columns with the IASI NH_3 total column observations. At the annual scale globally, the spatial correlation coefficient (r) between the yearly mean model-simulated NH_3 total columns and IASI observations improve from 0.71 (using prior emissions) to 0.90 (using IASI-constrained NH_3 emissions), while the RMSE decreases by ~29% from 0.52×10^{16} molec. cm^{-2} to 0.37×10^{16} molec. cm^{-2}. Similarly, at the monthly scale globally, the r value and RMSE between the model simulations with IASI-constrained NH_3 emissions and the IASI observations improve from 0.51 (using prior emissions) to 0.83 (using IASI-constrained NH_3 emissions), while the RMSE decreases by ~34% from 0.88×10^{16} molec. cm^{-2} to 0.58×10^{16} molec. cm^{-2}.

At the monthly scale and across major regions, including India, China, Africa, Europe, South America, and North America, the spatial correlation coefficients (r) and RMSE between the model simulations with estimated NH_3 emissions from inversions and the IASI observations are respectively much higher and smaller than when the simulations are based on the prior CEDS anthropogenic NH_3 emissions (Figure 4). The spatial correlation coefficient (r) between the IASI-constrained NH_3 emissions' model simulations of the NH_3 total columns and the IASI NH_3 observations exceeds ~0.8 in most of the regions at the monthly scale for this year 2019 of validation analysis (Figure 4). In one of the major NH_3 emitted regions, India, at the monthly scale, the spatial correlation increases from 0.40 to 0.86 and RMSE reduce by ~50% from 3.83×10^{16} molec. cm^{-2} to 1.91×10^{16} molec. cm^{-2} (Figure 4). Similarly, over another major NH_3 emission region, China, at the monthly scale, the spatial correlation increases from 0.40 to 0.79 and RMSE reduce by ~27% from 1.19×10^{16} molec. cm^{-2} to 0.87×10^{16} molec. cm^{-2} (Figure 4). It demonstrates the general improvement brought at different spatiotemporal scales by the update of the emission estimates from our inversions, and thus the internal consistency of our global inversion framework despite the rather simple linearization of the chemistry-transport underlying it. This improvement of the fit to the IASI NH_3 observations is a strong indication of the robustness of our inversion-based estimate of the global NH_3 emissions.

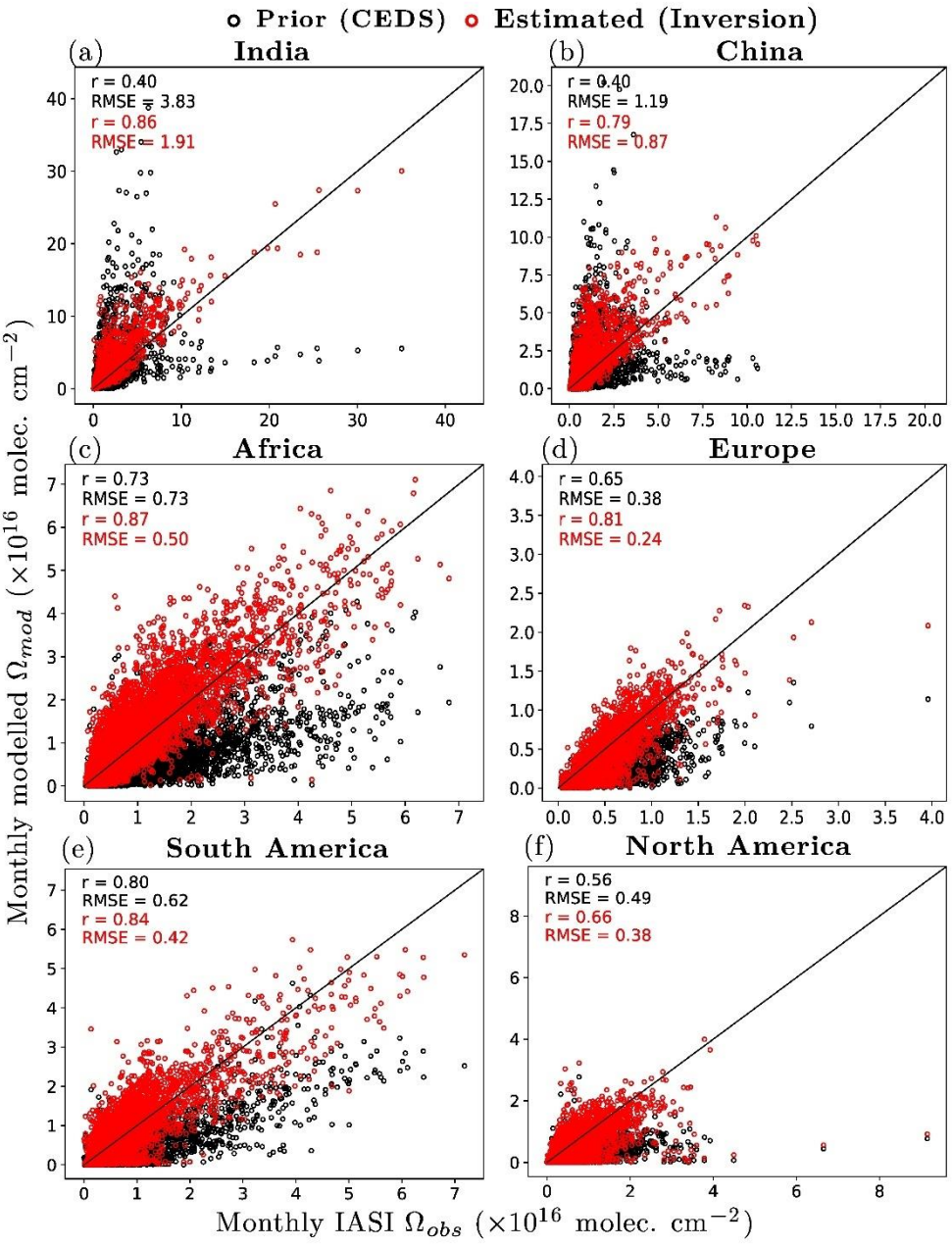

Figure 4: Comparison of the monthly averages of the IASI NH_3 column observations (Ω_{obs}) to the corresponding averages of these observations with two simulations of LMDZ-INCA (Ω_{mod}) using the IASI-constrained NH_3 emission estimates derived from our global inversions and using the prior CEDS NH_3 emissions over different regions for the year 2019. Each panel shows the correlation coefficient (r) and root mean square error (RMSE) between modeled (from both prior and IASI-constrained NH_3 emissions from inversions) and observed IASI NH_3 columns. The black line denotes the one-to-one line.

~~3.2~~3.3 IASI-constrained NH_3 emissions

~~Satellite data gaps, and some filters applied on observations and different variables in the FDMB inversion approach to focus on model grid cells dominated by anthropogenic NH_3 emissions (section 2.4), result in numerous grids or days where NH_3 emissions could not be derived directly from the IASI NH_3 observations. Therefore, the derivation of national or regional budgets of anthropogenic emissions at daily (10-day scale) to monthly and annual scale from the satellite observations requires a proper gap-filling of grid cell or days for which the inversion protocol does not yield emission estimates. To fill these gaps in IASI-constrained NH_3 emissions, we use a rather conservative approach utilizing IASI-constrained NH_3 emissions and the corresponding a priori CEDS anthropogenic NH_3 emissions used in the inversions. The gap-filling is performed over some specific regions. In order to gap-fill the daily unconstrained NH_3 emissions, we compute a daily scaling factor as a ratio between the IASI-constrained and the corresponding CEDS anthropogenic NH_3 emissions integrated over a specific region.~~

~~The missing emissions in that selected region are gap filled by multiplying in each corresponding grid cell the CEDS NH_3 emissions with these scaling factors. For a given day, when the spatial coverage of the IASI constrained anthropogenic NH_3 emissions is less than 60% in a specific region due to a poor satellite coverage and due to other data filtering to apply the FDMB inversion approach, we apply some constraints on the scaling factor to prevent spurious gap filled emissions. If the IASI constrained emissions coverage is less than 10%, we directly use the prior CEDS NH_3 emissions. For coverage between 10% and 40%, we cap the scaling factor at 1.25, and for coverage between 40% and 60%, we cap it at 1.5. For the gap filling, we use nine continental regions (illustrated in Figure S4) from the 10 regions defined by~~ Ge et al. (2022) ~~based on 58 IPCC reference regions representing consistent regional climate features described in~~ Iturbide et al. (2020). ~~Ge et al. (2022) used these nine regions to access global and regional budgets and fluxes of atmospheric reactive N and S gases and aerosols. The fraction of the IASI constrained and the gap filled NH_3 emissions per season across six regions for each year from 2019 to 2022 in Figure S5 shows that the gap filling of emissions over most of the regions is mostly higher during winter season and minimum during spring. However, in some regions such as India and Africa, the percentage of the gap filled emissions to the total seasonal emissions is higher in summer compared to other seasons due to relatively smaller numbers of satellite observations, caused by higher cloud coverage during the monsoon season. The overall percentage of the gap filled NH_3 emissions to the total emissions over worldwide is maximum (up to ~26%) during winter and minimum (up to ~10%) during spring season and it ranges from ~15% 18% during summer and autumn (Figure S5). However, since the attribution of the NH_3 emissions in winter season to the total annual emissions is smaller compared to other seasons, the total gap filled emissions in winter are still lower than in other seasons (Figure S6).~~

In the subsequent subsections, we present and discuss the~~se~~ gap-filled global daily (10-day scale) NH_3 emission estimates integrated on different temporal and spatial scales. Over the four-year period of our emission estimates, we present global and regional annual budgets, including the mean emissions over this period, with the range defining minimum and maximum annual emissions, as well as the variation of the regional estimates at different temporal scales ranging from daily (10-day scale) to monthly, seasonal, and annual.

~~3.2.1~~3.3.1 Global annual NH_3 emissions

The spatial distribution of the IASI-constrained annual NH_3 emissions averaged over the four-year period (2019-2022) in Figure 5~~4~~ (Figure S7~~5~~ for each year from 2019 to 2022) clearly reveals the main hotspots of the high anthropogenic NH_3 emissions over the globe on land areas. Figure 5~~4~~ shows that this four-years averaged annual IASI-constrained NH_3 emissions has a similar spatial distribution to the prior CEDS anthropogenic NH_3 emissions. However, over most of the major NH_3 emitting regions over the globe and over land areas, the IASI-constrained NH_3 emissions are higher compared to the prior CEDS emissions (Figure 5~~4~~). It shows that the ~~south~~ South and the ~~east~~ East Asian regions are the highest anthropogenic NH_3 emitting regions over the globe.

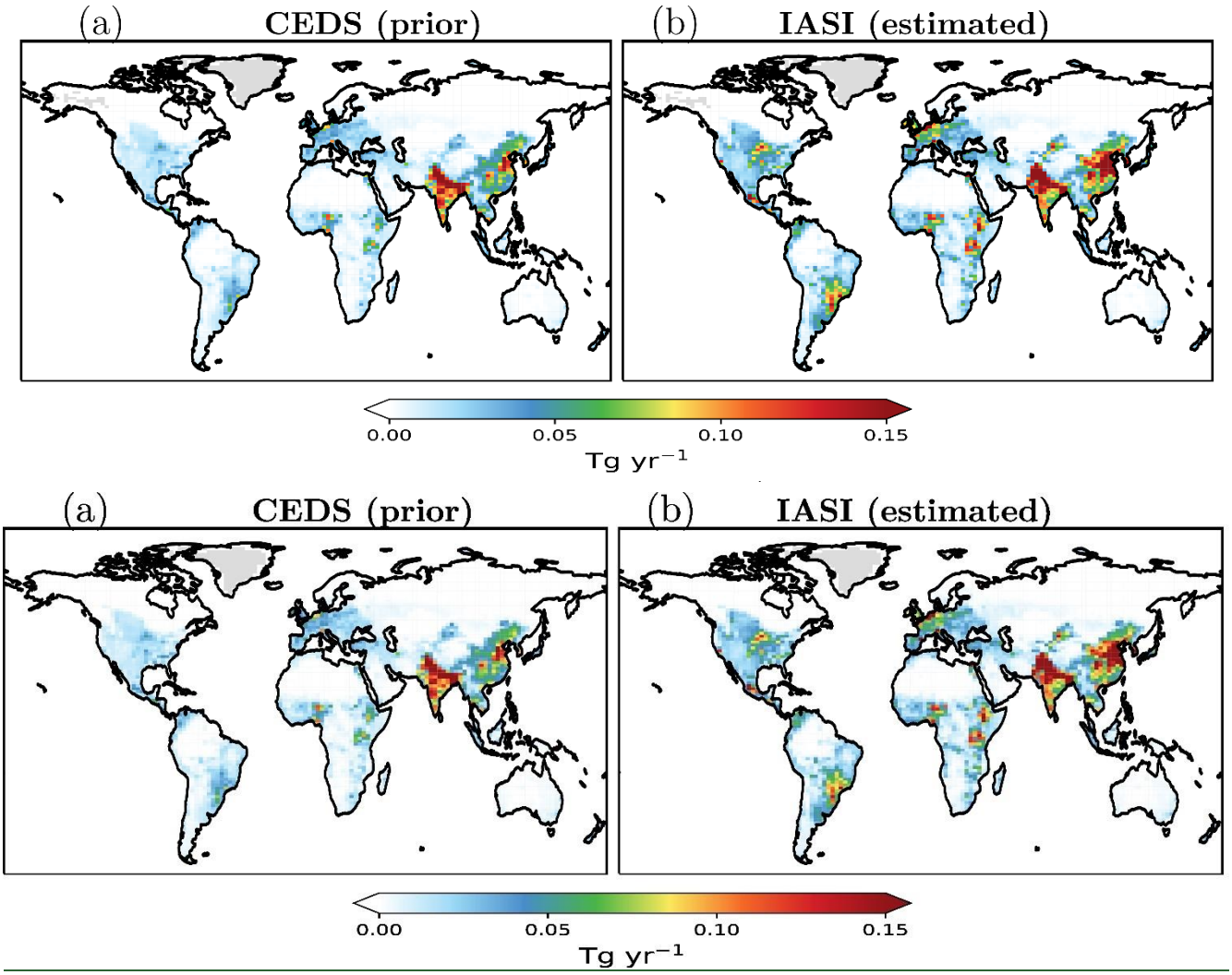

Figure 4~~5~~: Spatial distribution of the four-year (2019-2022) averaged annual NH_3 emissions, showing (a) the prior CEDS anthropogenic NH_3 emissions, and (b) IASI-constrained estimated NH_3 emissions from our global atmospheric inversions.

Figure 6~~5~~ presents the global annual IASI-constrained NH_3 emissions and its comparison with the prior CEDS anthropogenic NH_3 emissions for all the four years from 2019 to 2022. The slight differences in the prior CEDS emissions over the four years is mainly due to the different coverages of the dominating anthropogenic NH_3 emissions based on the CEDS anthropogenic and GFED's fire emissions (see section 2.4) and also some differences in the natural soil NH_3 emissions over the years. For each year, the IASI-constrained NH_3 emissions are higher than the prior CEDS emissions. The average of global annual NH_3 emission estimates over the four years period is ~~98~~ 97 (~~95~~93.~~0~~8-~~101~~99.~~4~~9) Tg yr^{-1}, which is ~~63~~61% (~~57~~55%-~~68~~65%) higher than the prior CEDS anthropogenic NH_3 emissions. The global annual NH_3 emission estimates show an increasing trend from the year 2019 to 2021 (Figure 6~~5~~). However, NH_3 emission estimates for 2022 (~~97~~ 96 Tg yr^{-1}) are lower than those for 2020 and 2021; however, still higher than those for 2019 (~~95~~ 94 Tg yr^{-1}).

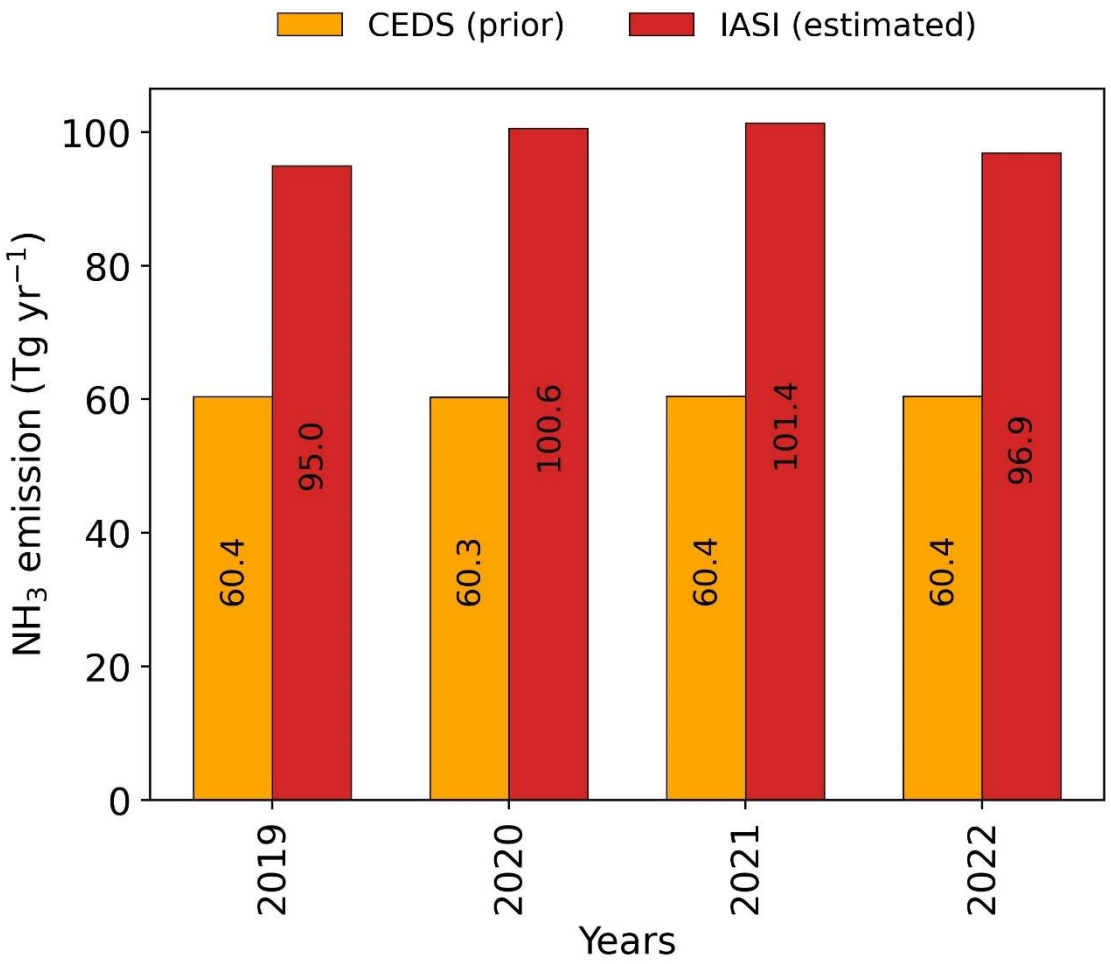
CEDS (prior)
IASI (estimated)
NH_3 emission (Tg yr^{-1})
0
20
40
60
80
100
60.4
95.0
60.3
100.6
60.4
101.4
60.4
96.9
2019
2020
2021
2022
Years

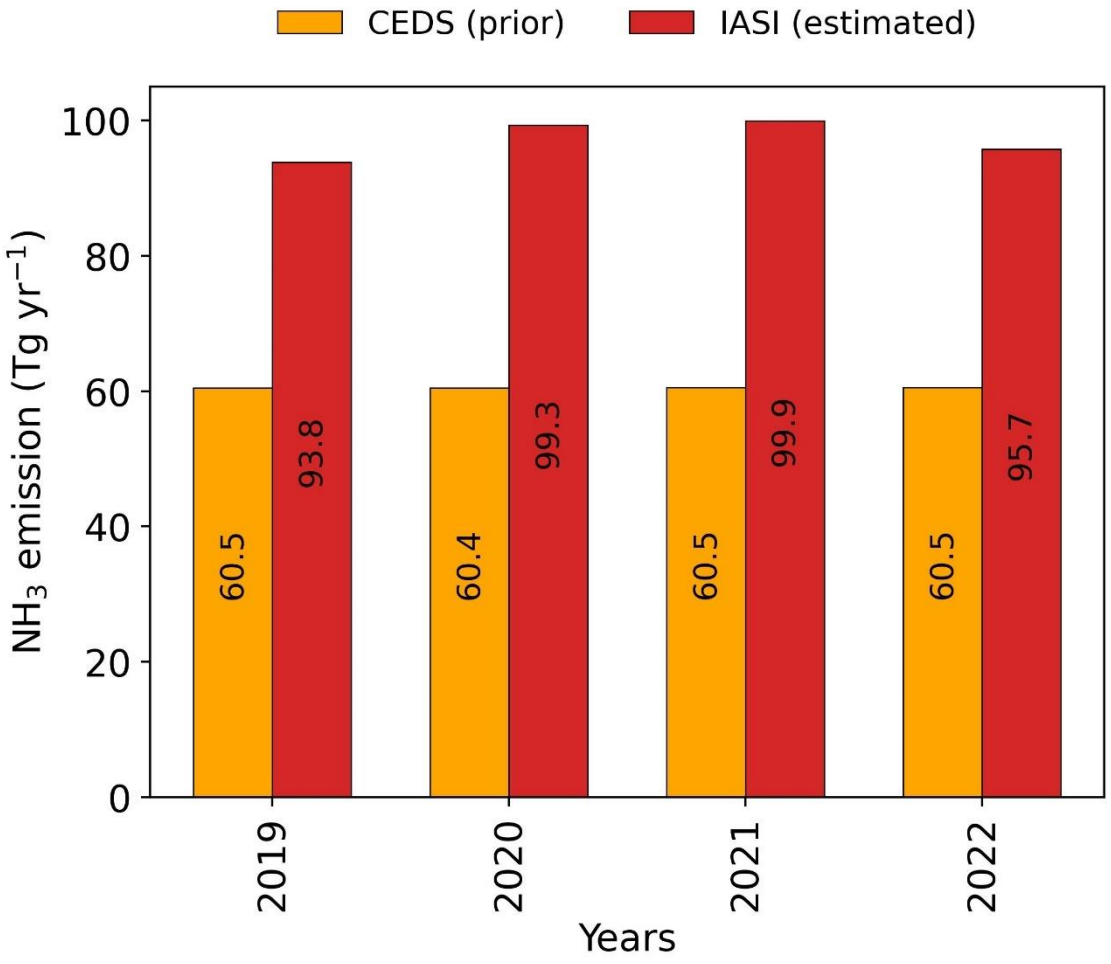
CEDS (prior)
IASI (estimated)
NH_3 emission (Tg yr^{-1})
0
20
40
60
80
100
60.5
93.8
60.4
99.3
60.5
99.9
60.5
95.7
2019
2020
2021
2022
Years

Figure 6~~5~~: Global annual NH_3 emissions for each year from 2019 to 2022, showing the prior CEDS anthropogenic NH_3 emissions (orange), and IASI-constrained (red) NH_3 emissions from inversions.

~~3.2.2~~3.3.2 Regional NH_3 emissions and seasonal variation

Figure 7~~6~~ illustrates the daily (at 10-day scale) variation of estimated NH_3 emissions for four years from 2019 to 2022 over the six specific regions, India, China, Africa, Europe, North America, and South America (defined in Figure S5~~2~~) which have the major anthropogenic ammonia emissions. In this figure, the prior CEDS anthropogenic NH_3 emissions of the year 2019 over the globe and over the land areas are almost the same in magnitudes and seasonal variation across the four years (Figure 6) and thus, the representation is shown only for the year 2019. Figure 8~~7~~ shows the spatial distributions of the four-year averaged annual IASI-constrained NH_3 emissions and the prior CEDS emissions over the six regions. The budgets of regional annual estimated and prior NH_3 emissions over the four years period for these selected regions are presented in Figure 9~~8~~.

The Indian and Chinese regions in the ~~south~~ South and ~~east~~ the East Asia are the major anthropogenic ammonia emitting regions in the world, with a majority of emissions originating from large crop-specific agriculture activities, including the use of synthetic fertilizers, manure, and emissions from soils and livestock. Over the Indian region, the highest NH_3 emission is from the Indo-Gangetic Plain region, which is attributed to the intensive agriculture practices (Figure ~~7~~8(a)). The average annual NH_3 emission estimates for the four-year period over the Indian region is ~15.~~1~~0 (14.4-15.~~5~~4) Tg yr^{-1} which is ~7% (~2%-10%) higher than the prior CEDS anthropogenic NH_3 emissions (~14.1 Tg yr^{-1}). The annual estimates over the Indian region show a slowly decreasing trend over the four-year period (Figure ~~8~~9(a)). Notably, the seasonal variation of the estimated NH_3 emissions across all the four years is similar to each other; however, it is always different from the prior CEDS NH_3 emissions (Figure 7~~6~~(a)). The seasonal variation in NH_3 emissions across different regions in the CEDS inventory dataset is rather coarse (Beaudor et al., 2023) and mostly based on the European practices of agricultural activities (Beale et al., 2022). The CEDS NH_3 emissions show two peaks in May and September, whereas, the estimates show the main peak in July and August and some small peaks from January to April for each inversion year. The high NH_3 emission estimates over the Indian region in July-August with a peak in July is consistent with the cropping cycle (dominatingly rice cultivation followed by corn), high usage of N-fertilizers, and high temperature during these monsoon and summer months in the Indo Gangetic Plain region. The high estimates in the winter and spring months can be attributed to the usage of N-fertilizers during the winter and spring crops seasons, particularly from the dominating wheat cultivation. Biomass burning is also a small contributing source of the NH_3 emissions in this region with the majority of fires resulting from crop-residue and stubble burning in the spring and autumn before replanting. Therefore, there should not be a significant problem of attribution between the anthropogenic and biomass burning emissions here.

The majority of IASI-constrained and the prior CEDS anthropogenic NH_3 emissions over the Chinese region are confined to the East China region (Figure 8~~7~~(b)). The four-year average of inverted annual NH_3 emission over the Chinese region is ~23.~~7~~4 (22.3~~5~~-~~25~~24.~~3~~9) Tg yr^{-1} (Figure ~~8~~9(b)). This averaged IASI-constrained NH_3 emission is ~~64~~62% (~~56~~54%-~~75~~72%) higher than the prior CEDS emissions (~14.5 Tg yr^{-1}) used in the inversions. For this region, we see an increasing trend in the estimated ammonia emissions from 2019 to 2021 (Figure ~~8~~9(b)). The annual NH_3 emission estimate for 2022 (23.2~~4~~ Tg yr^{-1}) is lower than those for maximum in 2021 (~24.9~~5~~ Tg yr^{-1}), comparable to those in 2020 (~23.3~~6~~ Tg yr^{-1}); however, it remains higher than those for 2019 (~22.3~~5~~ Tg yr^{-1}) (Figure 9~~8~~(b)). A majority of the ammonia emissions in this region originate from the crop-specific agriculture activities, more specifically the applications of synthetic fertilizer and livestock manure in different crop cultivations (Xu et al., 2018). The daily (at 10-day scale) variation of the NH_3 emissions in Figure ~~6~~7(b) shows a strong seasonality in the estimates across all the years over this region. The seasonality in the emission estimates across all the years is different from the prior CEDS NH_3 emissions used in the inversions. We observe mainly two high peaks in the estimates in spring (March-April) and in summer's June-July months, whereas the CEDS emissions show two peaks in May and September. The NH_3 emission estimates also show a small third peak in October for inversion years from 2020 to 2022, except for 2019.

The strong seasonality in the emission estimates in this region agrees well with the crop cycle when wheat cultivation dominates in spring and rice cultivation in the summer months (Xu et al., 2018)

As discussed before in section 3.1, seasonality in the CEDS inventory NH_3 emissions for most of the regions is mostly based European agricultural practices, corresponding to the fertilizers application before planting and after harvests (Beale et al., 2022). This does not accurately capture the NH_3 emissions in regions like China, India and the Middle East, where agriculture practices differ significantly (Beale et al., 2022; Chen et al., 2023a; Kuttippurath et al., 2020). Whereas, our inversion estimates based on the satellite data shows more realistic seasonality of NH_3 emissions across different regions, closely aligning with their respective crop and agriculture cycles.

South America, Africa, and North America regions are fire-dominated regions, particularly during the dry season when wildfires are prevalent (Figure S8) (Chen et al., 2023b). The biomass burning from the wildfires plays a significant role in contributing to the total ammonia emissions in these regions. When fire emissions attribution in the prior emissions used for inversion is inaccurate, the dominated anthropogenic emission grids are misrepresented. In contrast, IASI NH_3 observations will indicate high NH_3 emissions over these grid cells due to biomass burning. The recent release of the 5th version of the Global Fire Emissions Database (GFED5) indicates a 61% increase in global burned area compared to GFED4 (Chen et al., 2023b). This increase may result in anthropogenic NH_3 grids from the inversions corresponding to biomass burning grids, consequently revealing heightened anthropogenic dominated NH_3 emission estimates over these regions due to non-local contribution from transport from neighboring biomass burning dominating grids. Biomass burning generates NH_3 advection at higher altitudes which also breaks our assumption of weak lateral transport in FDMB inversion approach, which may attribute to large errors in the emission estimates over these regions.

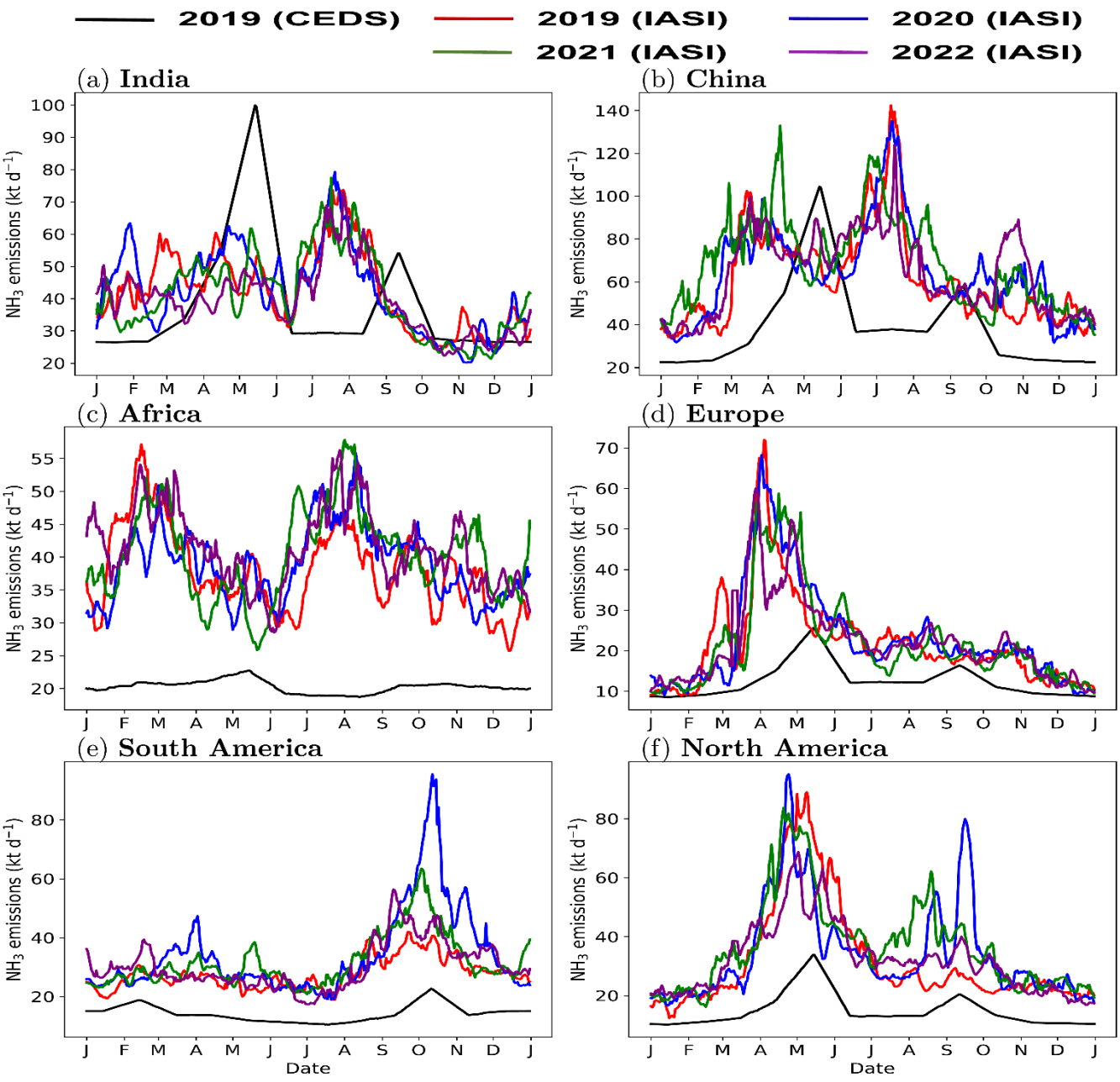
2019 (CEDS)
2019 (IASI)
2020 (IASI)
2021 (IASI)
2022 (IASI)
(a) India
(b) China
(c) Africa
(d) Europe
(e) South America
(f) North America
NH3 emissions (kt d−1)
J F M A M J J A S O N D J
Date

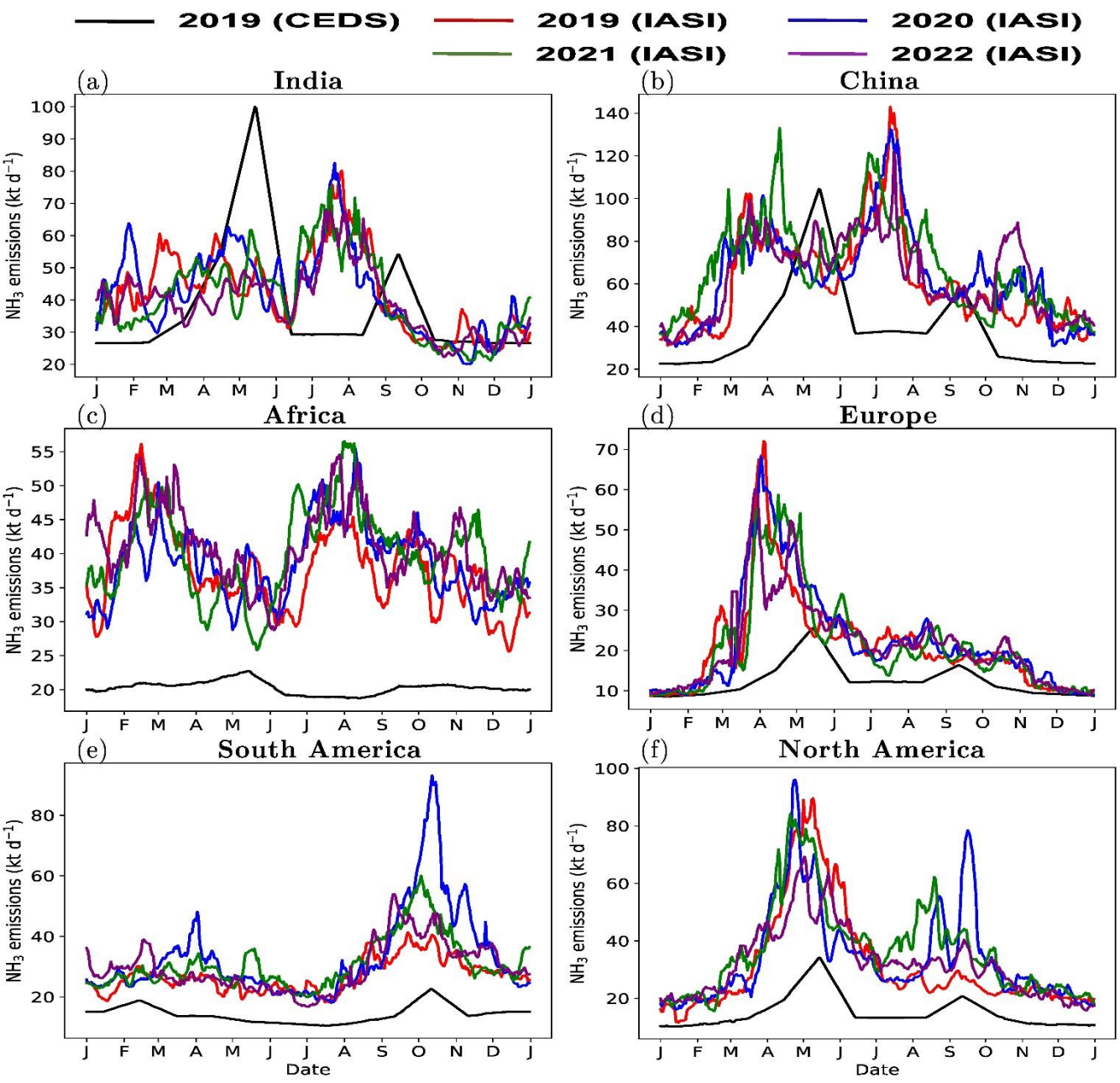

Figure 7: Daily (at 10-day scale) variation of the total estimated and the prior CEDS anthropogenic NH_3 emissions for the four years from 2019 to 2022 integrated over each selected region, (a) India, (b) China, (c) Africa, (d) Europe, (e) South America, and (f) North America.

For South American and African regions, our inversions respectively provide ~11.14 (~9.810.1-12.36) Tg yr^{-1} (Figure 8(e)) and ~14.45 (~13.8-1514.61) Tg yr^{-1} (Figure 98(c)) of the annual NH_3 emissions averaged over the four-year period. These averaged annual estimates for these regions exceed the prior CEDS emissions by approximately 2.12 and 2 times, respectively. Our estimates show a clear increasing trend in annual NH_3 emission over the Africa (Figure 89(c)). However, a decreasing trend of annual NH_3 emissions from 2020 to 2022 is observed over the South American region (Figure 89(e)). For the South American region, we observe a high peak in the estimated emissions during September to October months in each year and this peak in the year 2020 is much higher than that from other years (Figure 76(e)). In fact, the peak in 2021 is higher than the one from the estimates in 2019 and 2022. The seasonality of the estimates over the South American region is similar to the prior CEDS anthropogenic NH_3 emissions (Figure 76(e)). There was a high increase in number of fires in 2020 compared to other years in this region (Figure S8 (a)), which can also be observed from an enhanced observed NH_3 loading from IASI observations over this region in these years (Figure S63). The highest peak in the estimated NH_3 emissions in 2020 is mainly because of the contribution from these relatively higher number of fire occurrences in this year. For the African region, the

prior CEDS shows almost a flat seasonality relative to the estimates with a small peak in May; whereas, the estimates show at least two clear peaks in February-March and in July-August (Figure 7~~6~~(c)). The NH_3 emissions over this region remain high during other seasons also (Figure ~~6~~7(c)). Although we exclude grids dominated by the biomass burning emissions based on ~~from~~ the GFED4 bottom-up inventory in our inversions, mitigating its influence on the inversion estimates is challenging. This is due to the complexity arising from the fact that bottom-up NH_3 emissions lack the most updated information on fire occurrences, and the transport from biomass burning areas can extend to other regions, which is not accounted for in our inversion approach (Chen et al., 2023b).

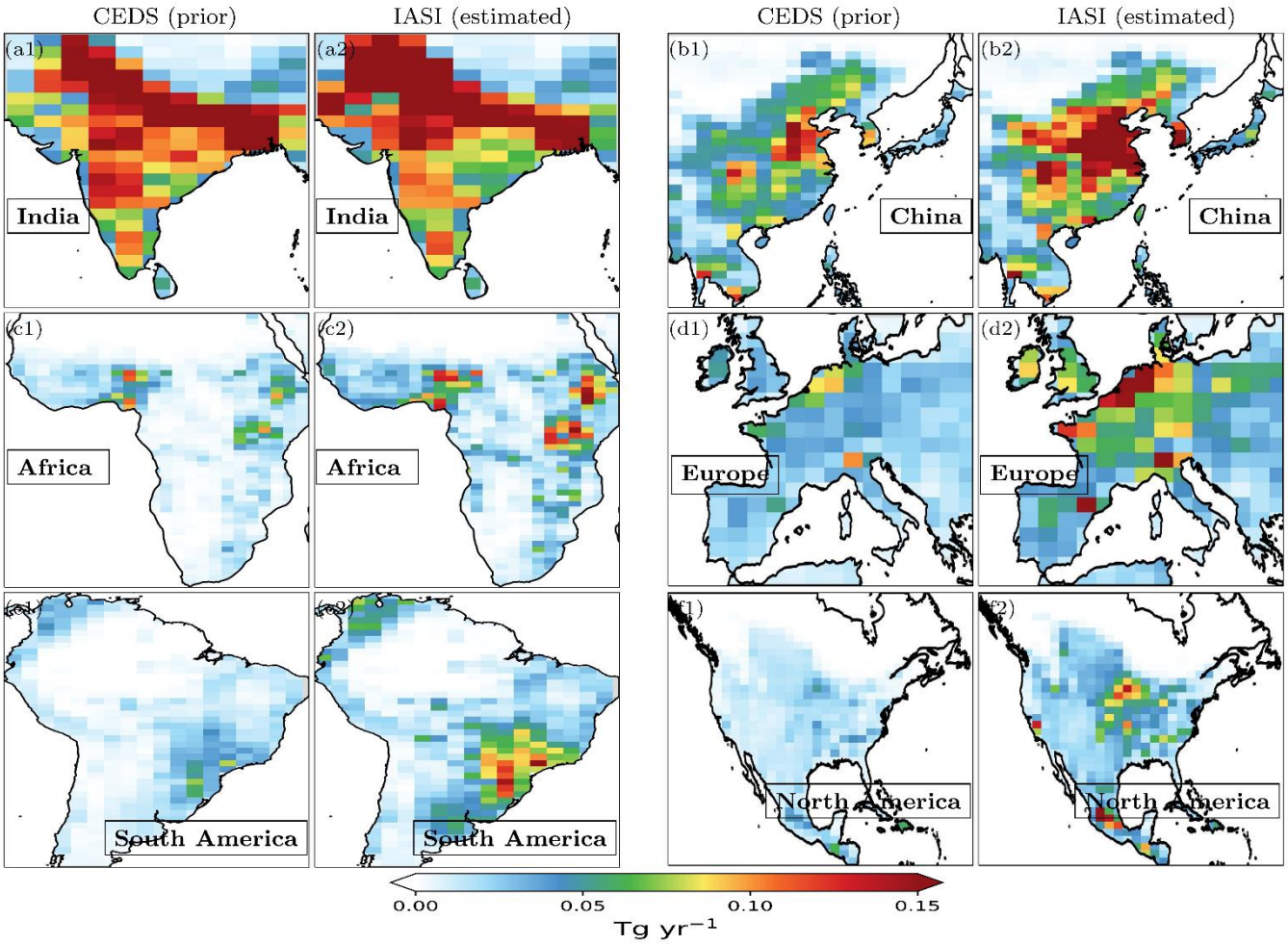
CEDS (prior)
IASI (estimated)
CEDS (prior)
IASI (estimated)
(a1)
(a2)
(b1)
(b2)
India
India
China
China
(c1)
(c2)
(d1)
(d2)
Africa
Africa
Europe
Europe
(e1)
(e2)
(f1)
(f2)
South America
South America
North America
North America
0.00
0.05
0.10
0.15
Tg yr⁻¹

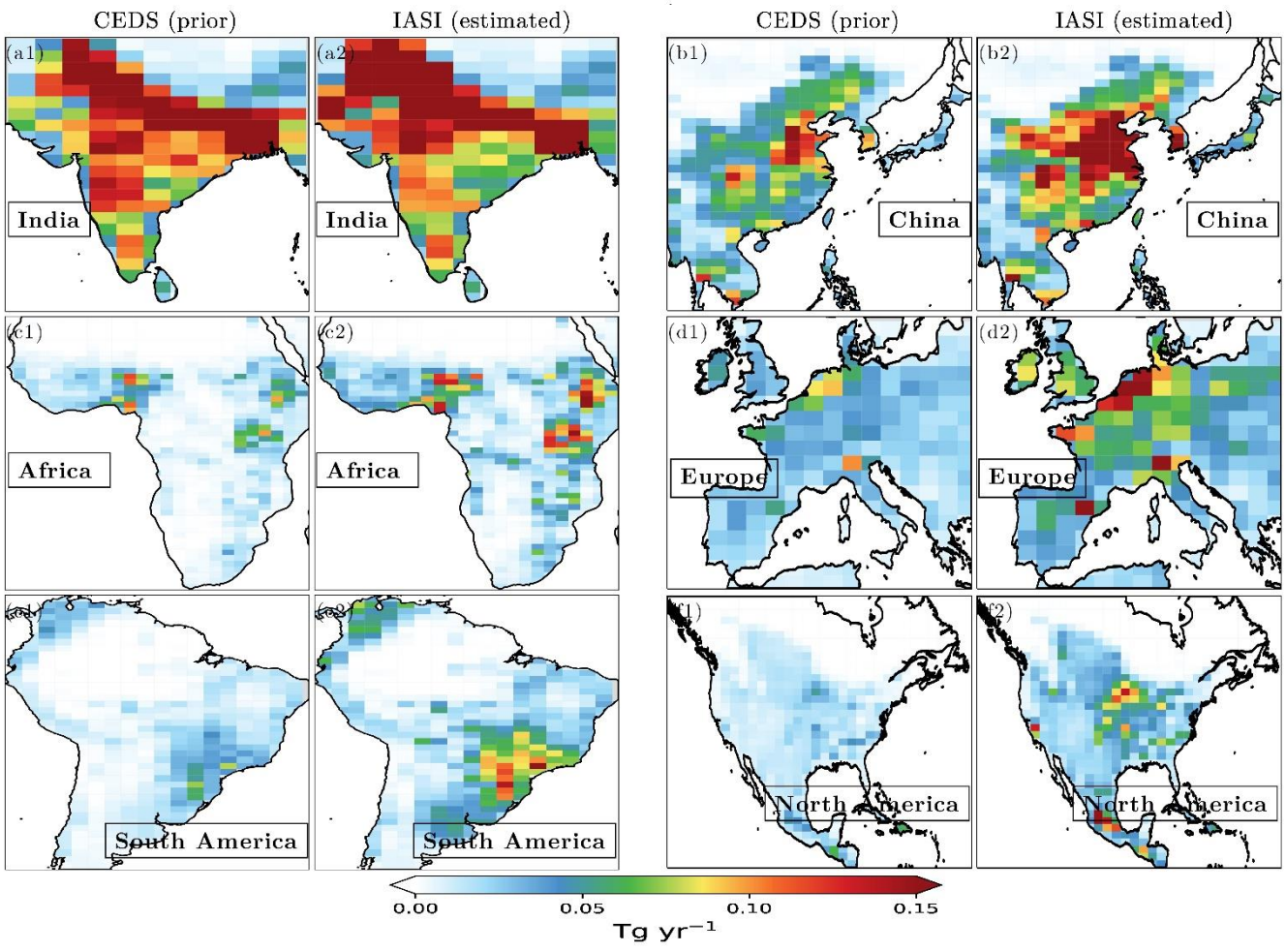
CEDS (prior)
IASI (estimated)
CEDS (prior)
IASI (estimated)
(a1)
(a2)
(b1)
(b2)
India
India
China
China
(c1)
(c2)
(d1)
(d2)
Africa
Africa
Europe
Europe
(e1)
(e2)
(f1)
(f2)
South America
South America
North America
North America
0.00
0.05
0.10
0.15
Tg yr⁻¹

Figure 87: Spatial distribution of the total annual NH_3 emissions averaged over the four years period (2019-2022) across six regions (a) India, (b) China, (c) Africa, (d) Europe, (e) North America, and (f) South America, showing bottom-up prior CEDS emissions (first column), IASI-constrained estimated emissions (E_{IASI}) using the IASI NH_3 observations ($\boldsymbol{\Omega_{obs}}$).

We estimate ~12.4 (11.67-13.45) Tg yr^{-1} four-year averaged annual NH_3 emissions over the North American region which is approximately 2.23 times higher than the prior CEDS anthropogenic NH_3 emissions (Figure 98(f)). Our inversion estimates show an increasing trend of annual NH_3 emissions from 2019 to 2021 over this region, but 2022 estimates are smaller than those from 2020 and 2021 and comparable to the 2019 emissions (Figure 98(f)). The estimates show a strong seasonality with peak emissions in April-May across all the years (Figure 67(f)). For the years 2020 to 2022, especially for 2020 and 2021, we observed a secondary peak during August and September which is less visible in 2019 emissions. The high secondary peak in 2020 and 2021, may result from an increased biomass burning due to more wildfires in these years compared to 2019. Similar to the South American and African regions, in North American region also, the impact of biomass burning from fires from some regions may contribute to the higher ammonia emissions (Figure S8(c)). In fact, the highest peak in the estimated emissions in 2020 in this region corresponds to an extreme cluster of wildfire events known as the "August Complex Fire" in 2020. This event originated as 38 separate fires started by lightning strikes on August 16-17, 2020, in the western U.S., leading to the first "gigafire" event in modern history in California (Campbell et al., 2022; Makkaroon et al., 2023). Campbell et al. (2022) showed that this 2020 "gigafire" contributed up to 83% of the total nitrogen emissions in the western U.S. However, based on GFED4 inventory fire emissions, our inversion could not filter out the grids dominated by these wildfire emissions during such events in this region.

Over the European region, hotspot regions with high anthropogenic NH_3 emissions are well detected for our inversion estimates (Figure 87(d)). The four-year averaged of annual NH_3 emission estimates over this region is estimated as ~7.98.2 (7.78.0-8.25) Tg yr^{-1} (Figure 98(d)). The estimated annual emissions over this region in 2020 are higher than in the other remaining inversion years; however, the estimates still remain approximately comparable across these years (Figure 98(d)). Our emission estimates over the European region are ~7288% higher compared to the prior CEDS anthropogenic NH_3 emissions. The estimates show a strong seasonality across all the years, with high emissions from March to May with a peak in April (Figure 76(d)). This seasonality in the estimates differs from the prior CEDS anthropogenic NH_3 emissions which show a high peak in May and a smaller one in September (Figure 76(d)). The strong seasonality in the emission estimates agrees well with the crop cycle over the European region when the main cultivation activities dominate in the spring and summer seasons.

Other than these selected regions, we also briefly analyzed regional estimates over the Middle East region, a comparatively smaller ammonia emitting region (Figure S9). A recent study by Osipov et al. (2022) based on ship-borne measurements around the Arabian Peninsula and modelling showed that NH_3 emissions over the Middle East region are significantly underestimated, potentially by a factor exceeding 15 from EDGAR inventory emission used in their model simulations. While natural sources of ammonia play a negligible role in this region, the vast majority of emissions arise from industrial and agricultural activities. Over the Middle East region, our average annual anthropogenic estimate of ~4.54 Tg yr^{-1} (~4.4-4.5 Tg yr^{-1}) is approximately 5049% higher than the prior CEDS emissions (~3.0 Tg yr^{-1}). The annual NH_3 emissions in these regions remained almost the same over the four-year period (Figure S9(c)). The estimated NH_3 emissions show strong seasonality with a high peak in May-April and a second peak in July-August across all the four years, whereas, the prior CEDS anthropogenic NH_3 emissions show two peaks in May and September (Figure S9(b)).

4 Discussion

4.1 Comparison with bottom-up inventories and other NH_3 emissions estimates

We compare in this section our IASI-inverted NH_3 emission estimates with other global and regional bottom-up inventories, as well as with other available NH_3 emissions inversion estimates reported in the recent literature. We use two global bottom-

up NH_3 emission inventories (i) CAMS-GLOB-ANT v6.2 (developed by combining the CEDSv2 emissions trends and temporal profiles from CAMS-GLOB-TEMPO and EDGAR v6 historical monthly NH_3 emission data up to 2018) 0.1°×0.1° monthly dataset (Granier et al., 2019; Soulie et al., 2023) from 2019 to 2022, and (ii) the process-based agricultural and natural soil NH_3 emissions from the Calculation of AMmonia Emissions in ORCHIDEE (CAMEO) model at 1.27°×2.5° horizontal and monthly temporal resolutions (Beaudor et al., 2023). CAMEO simulates NH_3 sources from the agricultural sector, from livestock manure management (including animal housing and manure storage to grazing) to synthetic and organic nitrogen application to soil. Since CAMEO emissions are not only limited to cultivated / livestock areas and are dynamically dependent on environmental conditions and atmospheric deposition, emissions from natural ecosystems are also exploited in this study. For these inter-comparisons, we re-gridded the global NH_3 emissions from the bottom-up inventories on the grids (1.27°×2.5°) of our estimated emissions. We also sub-sampled the monthly emissions from the bottom-up inventories on the common grids corresponding to the IASI-constrained monthly NH_3 emissions derived from the daily (at 10-day scale) estimates. Note that CAMEO additionally includes natural soil NH_3 emissions; whereas, CAMS emissions do not include it and provide only anthropogenic NH_3 emissions.

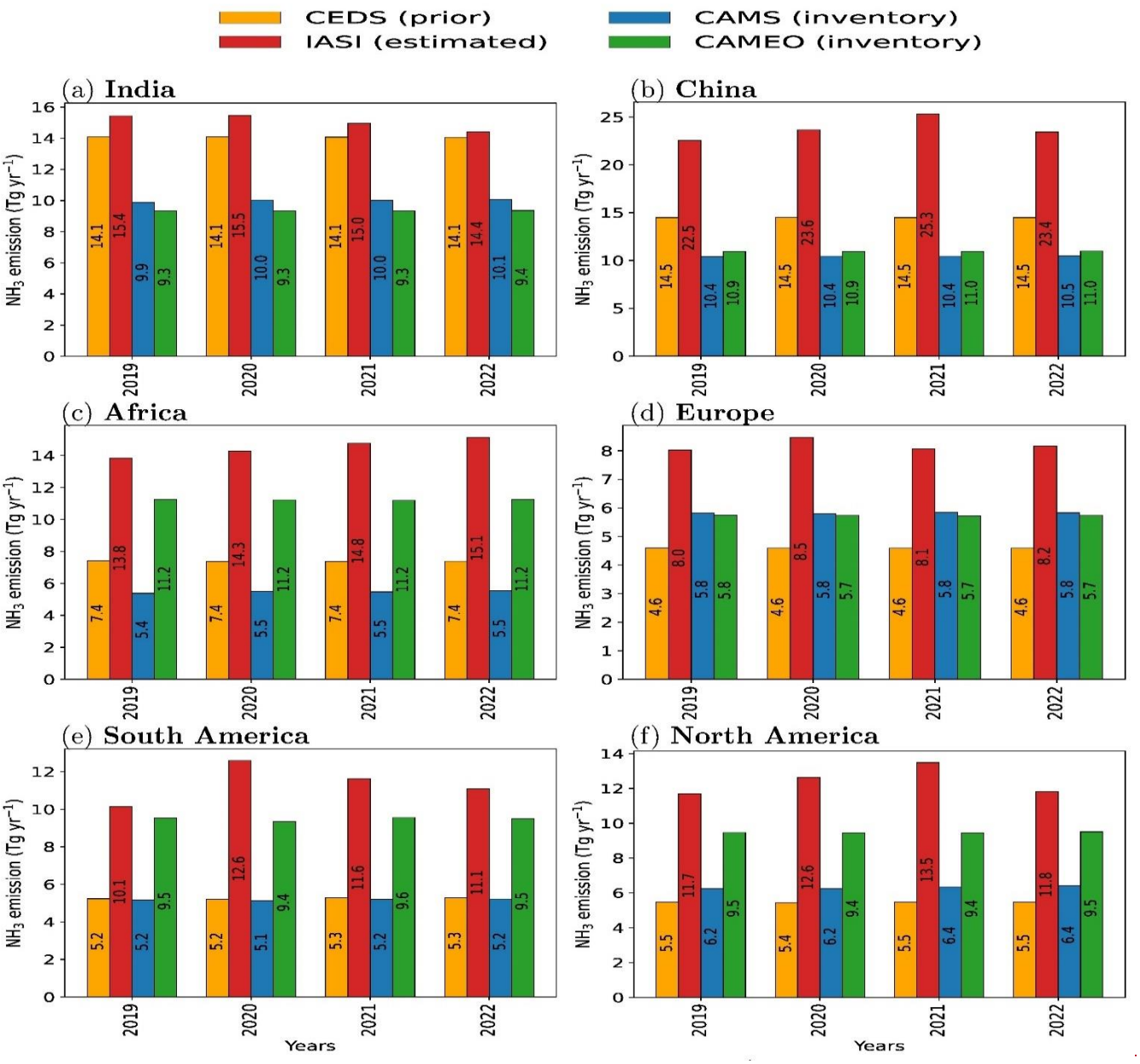
CEDS (prior)
IASI (estimated)
CAMS (inventory)
CAMEO (inventory)
(a) India
(b) China
(c) Africa
(d) Europe
(e) South America
(f) North America
NH3 emission (Tg yr−1)
Years
2019
2020
2021
2022
14.1 15.4 9.9 9.3
14.1 15.5 10.0 9.3
14.1 15.0 10.0 9.3
14.1 14.4 10.1 9.4
14.5 22.5 10.4 10.9
14.5 23.6 10.4 10.9
14.5 25.3 10.4 11.0
14.5 23.4 10.5 11.0
7.4 13.8 5.4 11.2
7.4 14.3 5.5 11.2
7.4 14.8 5.5 11.2
7.4 15.1 5.5 11.2
4.6 8.0 5.8 5.8
4.6 8.5 5.8 5.7
4.6 8.1 5.8 5.7
4.6 8.2 5.8 5.7
5.2 10.1 5.2 9.5
5.2 12.6 5.1 9.4
5.3 11.6 5.2 9.6
5.3 11.1 5.2 9.5
5.5 11.7 6.2 9.5
5.4 12.6 6.2 9.4
5.5 13.5 6.4 9.4
5.5 11.8 6.4 9.5

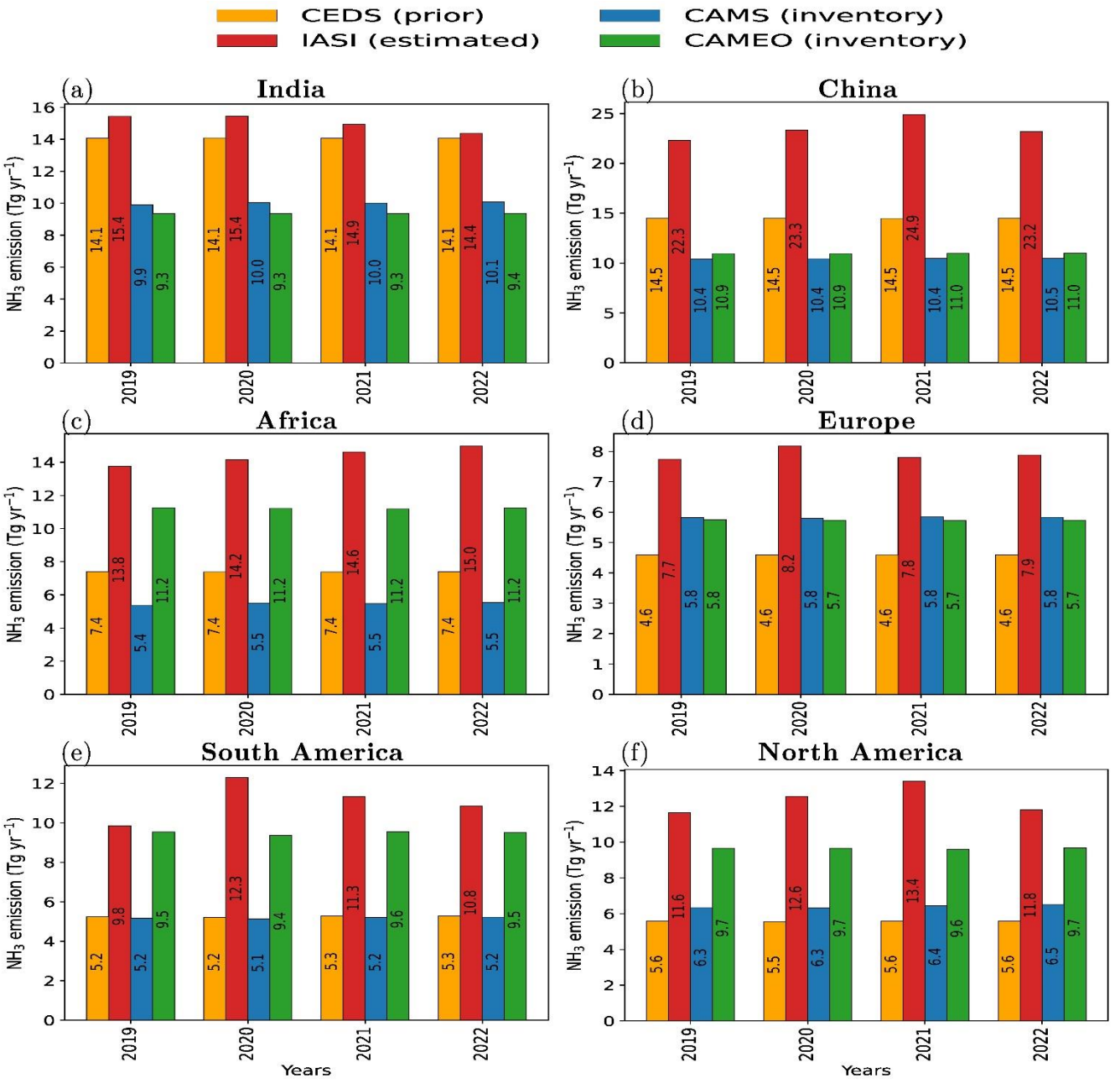

735 **Figure- 98:** The regional annual NH_3 emissions spanning from 2019 to 2022 over the six regions over the land areas, derived from the IASI-constrained daily global estimates, the prior CEDS inventory anthropogenic NH_3 emissions, and two independent global bottom-up inventories CAMS (anthropogenic NH_3 emissions) and CAMEO (combined agriculture and natural soil NH_3 emissions). The CAMEO NH_3 emissions is for its last available year, 2014 selected on the common grids of each year's estimates.

740 The four-year (2019-2022) averaged of the ~~G~~global annual anthropogenic NH_3 emissions from CAMS bottom-up inventory (~52.5~~4~~ Tg yr^{-1}), subsampled on the common grids where IASI-constrained monthly emissions are available, are lower than the prior CEDS anthropogenic NH_3 emissions (~60.5~~4~~ Tg yr^{-1}); whereas, global annual NH_3 emission from CAMEO from combined agricultural and natural soil sectors (~71.1 Tg yr^{-1}) are higher than those from both CEDS and CAMS. Therefore, we have even larger relative difference between the estimated and the CAMS emissions than the relative difference between
745 the estimated and CEDS emissions (Figure ~~8~~9). However, this relative difference between the estimated and CAMEO's combined agriculture and natural soil NH_3 emissions are smaller compared to the relative difference between the estimated and CEDS. The four-year averaged global annual NH_3 emissions from the inversions are ~1.8~~9~~ times higher than CAMS anthropogenic NH_3 emissions and ~1.4 times higher than CAMEO combined agriculture and natural soil NH_3 emissions. Figure ~~8~~ 9 shows a comparison between the IASI-inverted annual emissions and corresponding CAMS and CAMEO emissions

over six regions (and over the Middle in Figure S9) and across four years, revealing consistently higher IASI-constrained emissions compared to these global bottom-up inventories.

We also compare our estimates with the recent global NH_3 inversion emission estimates by Luo et al. (2022) based on a previous version of IASI NH_3 observations from 2008 to 2018, with the recent estimates from Dammers et al. (2022) derived using the CrIS observations from 2013 to 2020, and with some other regional inversion estimates. Luo et al. (2022) estimated global annual NH_3 emissions at ~78 (70-92) Tg yr^{-1} averaged over a period from 2008 to 2018, and Dammers et al. (2022) over a period from 2013 to 2020 had 216.6±66.2 Tg yr^{-1} (for all detected source locations) and 74.1±17.7 Tg yr^{-1} (for inventory identified source locations). Our averaged global annual NH_3 emissions estimates of ~978 (945~~-101~~100) Tg yr^{-1} from 2019 to 2022 are ~~26~~25% higher compared to the average total estimates (~78 Tg yr^{-1}) from Luo et al. (2022). This can partly be explained by the fact that the IASI version 4 NH_3 column values used in this study are also about 10-20% higher than the earlier version 3 (Clarisse et al., 2023) used by Luo et al. (2022) due to a reduction of the retrieval biases. This also has to be explained by the use of a different inversion approach, of a different chemistry transport model, and application of ~~averaging kernel~~AKs from IASI NH_3 observations to model simulated NH_3 columns in this study. Our estimates align more closely with the upper range (~92 Tg yr^{-1}) of their emission estimates obtained by setting a 200% perturbation to the modelled atmospheric NH_3 lifetime in their inversions. It should be noted that Luo et al. (2022) corrected their NH_3 emissions over the Indian and the East China regions during 2013 to 2018, which were impacted by the rapid changes in SO_2 emissions and concentrations in these regions, especially rapidly decrease of SO_2 emissions over China. A decrease in SO_2 emissions leads to an increase in NH_3 concentrations/columns in the troposphere because lower SO_2 levels reduce the formation of ammonium sulfate aerosols, leaving more free ammonia in the atmosphere, which increases its concentration in the air (Luo et al., 2022). This correction in Luo et al. (2022) leads to a small increase in NH_3 emissions over the Indian region. However, a substantial reduction of ~7-8 Tg for the year 2018 is observed over the East China region. Without any correction for SO_2 trends, our estimates (for 2019) are closer to their estimates for the year 2018. In contrast, our average total global estimate of ~978 (935.~~0~~8~~-101.4~~99.9) Tg yr^{-1} for the period 2019-2022 is ~2.2 times smaller than the 216.6±66.2 Tg yr^{-1} total from the sum of all detected source estimates from Dammers et al. (2022). Additionally, our four-year averaged estimates are ~313% higher when comparing with their estimates (74.1±17.7 Tg yr^{-1}) corresponding to the sources in CAMS-GLOB-ANT v4.2 inventory emissions above the detection limit of their satellite-constrained emissions.

In order to compare our regional NH_3 emissions, derived from the global inversion estimates, with those of Luo et al. (2022), we re-gridded their final inversion year (2018) estimates to match the spatial resolution (1.27°×2.5°) of our estimated NH_3 emissions. Subsequently, we integrate both the emission estimates over the identical grids on common selected regions' domains over the land and compare their final inversion year's (2018) NH_3 emissions with our nearest first inversion year (2019) estimates. For comparison with Dammers et al. (2022), their regional estimates for all detected source locations are consistently higher than our estimates. Therefore, in the subsequent comparison analysis, we compare our estimates only with their regional reported estimates corresponding to the sources with inventory emissions above the detection limit of their satellite-derived emissions. This comparison is consistent as our estimates also required information on the prior CEDS NH_3 emissions and for the missing sources with zero emissions in bottom-up inventory, our inversion will not detect any new emission sources. Over the Indian region, our annual estimates of 2019 (~15.4 Tg yr^{-1}) are closer to the estimates of 2018 (~13.1 Tg yr^{-1}) from Luo et al. (2022), representing a marginal ~183% increase. Our estimates over the China region of 2019 (22.3~~5~~ Tg yr^{-1}) are much higher (~73~~5~~%) compared to Luo et al. (2022) SO_2 trend corrected NH_3 emissions (~13 Tg yr^{-1}); however, these are closer to their estimates without correction. Recently, Liu et al. (2022) estimated 21.6 Tg NH_3 yr^{-1} (≡ 17.77 Tg N yr^{-1}) annual emissions over China for the year 2019 using satellite data and our estimates (22.3~~5~~ Tg yr^{-1}) for the same year are comparable to these inversion estimates. Dammers et al. (2022) reported ~35 Tg yr^{-1} averaged NH_3 emissions for the Asia region and our combined four-year averaged estimate of ~43 Tg yr^{-1} from India, China, and the Middle East regions is

~2423% higher than their estimate. Our estimates for Africa (~13.8 Tg yr^{-1}), South America (~9.810.1 Tg yr^{-1}), and the Middle East (~4.4 Tg yr^{-1}) regions for 2019 agree well with Luo et al. (2022) estimates (11.1 Tg yr^{-1}, 10.5 Tg yr^{-1}, and 4.1 Tg yr^{-1}, respectively) for of 2018 within ~24%, ~64%, and ~67%, respectively. For the South American region, our annual estimate of ~9.810.1 Tg yr^{-1} for 2019 agrees well with the estimate of 9.1 Tg yr^{-1} from Dammers et al. (2022). Our estimates (11.67 Tg yr^{-1}) for 2019 over the North American region are ~55% higher than ~7.5 Tg yr^{-1} from Luo et al. (2022); however, they are closer comparable to the total estimates of 12.2 Tg yr^{-1} from Dammers et al. (2022). Recently, Sahoo et al. (2024) constructed a high-resolution gridded (0.1° × 0.1°) emission inventory of NH_3 emissions over India for 2022 by including 24 regional major and minor anthropogenic sources. They estimated 10.54 Tg yr^{-1} of NH_3 emissions in 2022, which are closer to the CAMS anthropogenic NH3 emissions, while our inversion estimates of 15.514.4 Tg yr^{-1} NH_3 emissions for the same year are ~4236% higher than their estimates (Figure 89(b)). However, in this comparison analysis over the Indian region, our selected domain is larger, encompassing most of South Asia, compared to the India-only domain considered in Sahoo et al. (2024).

Over the European region, our annual NH_3 estimate (~7.78 Tg yr^{-1}) for 2019 is ~9188% higher compared to ~4.1 Tg yr^{-1} from Luo et al. (2022) for 2018. However, our four-year averaged annual estimates (~7.98.2 Tg yr^{-1}) are ~2966% smaller than ~11.1 Tg yr^{-1} from the estimates of Dammers et al. (2022). The European Union (EU) emission inventory report (EEA Report No 4/2023, 2023) reported comparatively lower NH_3 emissions for EU 27-member states as 3.5 Tg yr^{-1}, 3.4 Tg yr^{-1} and 3.3 Tg yr^{-1} for 2019, 2020, and 2021, respectively, which are much lower compared to our estimates for these years. Also, some other recent top-down inversion studies, such as (Tichý et al., 2023) have obtained a similar order of the magnitude of the emissions (4.3 Tg yr^{-1} and 4.0 Tg yr^{-1} for 2019 and 2020, respectively) using the CrIS satellite observations as from Luo et al. (2022) (4.1 Tg yr^{-1} for 2018) or from (EEA Report No 4/2023, 2023). However, our estimates are comparable to the NH_3 emissions derived from a recent regional atmospheric inversion over Europe at 0.2°×0.2° horizontal and monthly temporal resolutions over a three year period from 2020 to 2022, derived within the EU project Sentinel EO-based Emission and Deposition Service (SEEDS) (https://www.seedsproject.eu/data/monthly-nh3-emissions) (Ding et al., 2020, 2024). In this regional atmospheric inversion, NH_3 emissions over Europe were derived by DECSO (Daily Emissions Constrained by Satellite Observations) v6.2 algorithm, developed to derive emissions of short-lived species based on an extended Kalman Filter approach and using CrIS (NOAA-20) observations (Ding et al., 2020, 2024). Our annual NH_3 emission estimates integrated over the common European domain [10°W-30° E, 35°N-55° N] of their inversions, amounting to 8.89.1 Tg yr^{-1}, 8.47 Tg yr^{-1}, 8.7 4 Tg yr^{-1} for three years 2020, 2021, and 2022, respectively, are in good agreement (within ~1-812%) with 8.2 Tg yr^{-1}, 8.4 Tg yr^{-1}, and 8.6 Tg yr^{-1} derived for the same years in SEEDS NH_3 emission inversions. SEEDS NH_3 emission estimates over Europe indicate an increasing trend of ~0.2 Tg yr^{-1} over a three-year period from 2020 to 2022. In contrast, our inversion estimates show a peak in 2020, with comparatively slightly lower values in the subsequent years (Figure 98(d)).

This comparison analysis show that our inversion estimates of NH_3 emissions integrated at global or regional spatial scales are within the range of other previous inversion estimates derived based on different satellite observations and different inversion approaches. When comparing our IASI-based inversion estimates with some of those derived from CrIS observations, the differences in satellite overpass times (IASI ~09:30 LST, CrIS ~13:30 LST) could also lead to differences in retrieved NH_3 due to the potentially strong and quite uncertain diurnal variability in NH_3 emissions and atmospheric concentrations and retrieval approaches. However, in the current setup of our model (LMDZ-INCA), the anthropogenic NH_3 emissions are derived from a 1-month resolution inventory which is uniformly distributed in time at the hourly resolution, without incorporating diurnal cycles. This lack of diurnal variations in the input prior emissions could indeed enhance the discrepancies between IASI- and CrIS-based emission estimates. In a study by (Dammers et al., 2019), they utilized both IASI and CrIS satellites observations to estimate NH_3 emissions, lifetimes, and plume widths from major agricultural and industrial point sources. Their findings indicate that CrIS-derived emission estimates are, on average, slightly higher than those obtained from IASI-A and IASI-B observations. However, these differences remain within the overall uncertainty range of the estimates. The

differences in the emissions from CrIS and IASI could be due to the bias between the satellite NH_3 retrievals, as well as the potential influence of the different overpass times of these satellites in combination with the strong diurnal cycles of the emissions. Overall, ~~O~~our estimates, as well as these other inversion estimates, are higher compared to the NH_3 emissions from different global or regional bottom-up inventories, which tend to support the assumption that there is a general underestimation of the emissions in the inventories. The bottom-up inventories do not accurately capture the seasonality of NH_3 emissions in relation to the agricultural and crops activity cycles in some regions like India, China and the Middle East. In contrast, our inversion estimates demonstrate a seasonality that is consistent with the crops and agriculture cycles in these regions.

4.2 Impact of COVID-19 lockdowns on NH_3 emissions

The strict restrictions imposed during the COVID-19 lockdown periods in the year 2020 across different regions/countries/cities around the world observed major changes in anthropogenic activities, atmospheric concentrations, and emissions of different air pollutant species like NOx and SO_2. However, atmospheric NH_3 concentration and emissions received comparatively less attention compared to NOx or SO_2 and only a very few studies analyzed the impact of COVID lockdowns on ambient NH_3 concentrations. Most of the air pollutants like NOx and SO_2 show a decline in their atmospheric concentrations and emissions during COVID-19 lockdown periods (Zheng et al., 2021). The decline in NOx and SO_2 concentrations in the atmosphere during the COVID-19 lockdowns leads to reduction of formation of ammonium nitrate and ammonium sulfate aerosols from atmospheric ammonia, and hence a decrease in the atmospheric sink of NH_3. Meanwhile, agriculture activities remained mostly unchanged during COVID-19 lockdown periods. These factors along with changes in meteorology and atmospheric composition may have impacted ammonia levels in the atmosphere. A recent study by Kuttippurath et al. (2024) showed that the global atmospheric ammonia concentration increased anomalously almost everywhere around the world during COVID-19 lockdown periods in the year 2020 compared to the previous year 2019. Some other studies at regional or city scale, e.g., Xu et al. (2022) (China), Viatte et al. (2021) (Paris in France), Lovarelli et al. (2021) (Lombardy region in Italy), also reported increase of ammonia concentration in the atmosphere during COVID-19 lockdown periods in 2020. Recently, Evangeliou et al. (2024) conducted inversion estimates of NH_3 emissions based on satellite observations during the COVID-19 lockdowns in Europe and shown that the NH_3 emissions decreased by ~9.8% in the first half of the 2020 compared to 2016-2019. However, overall atmospheric ammonia levels increased due to reduced chemical removal from lower SO_2 and NOx emissions and the persistence of agricultural activity (Evangeliou et al., 2024). In this study, we analysed the changes in estimated daily (at 10-day scale) NH_3 emissions from our global inversions during COVID-19 major lockdowns in 2020 compared to the estimates during the same period in pre-COVID year 2019 over six regions across the world.

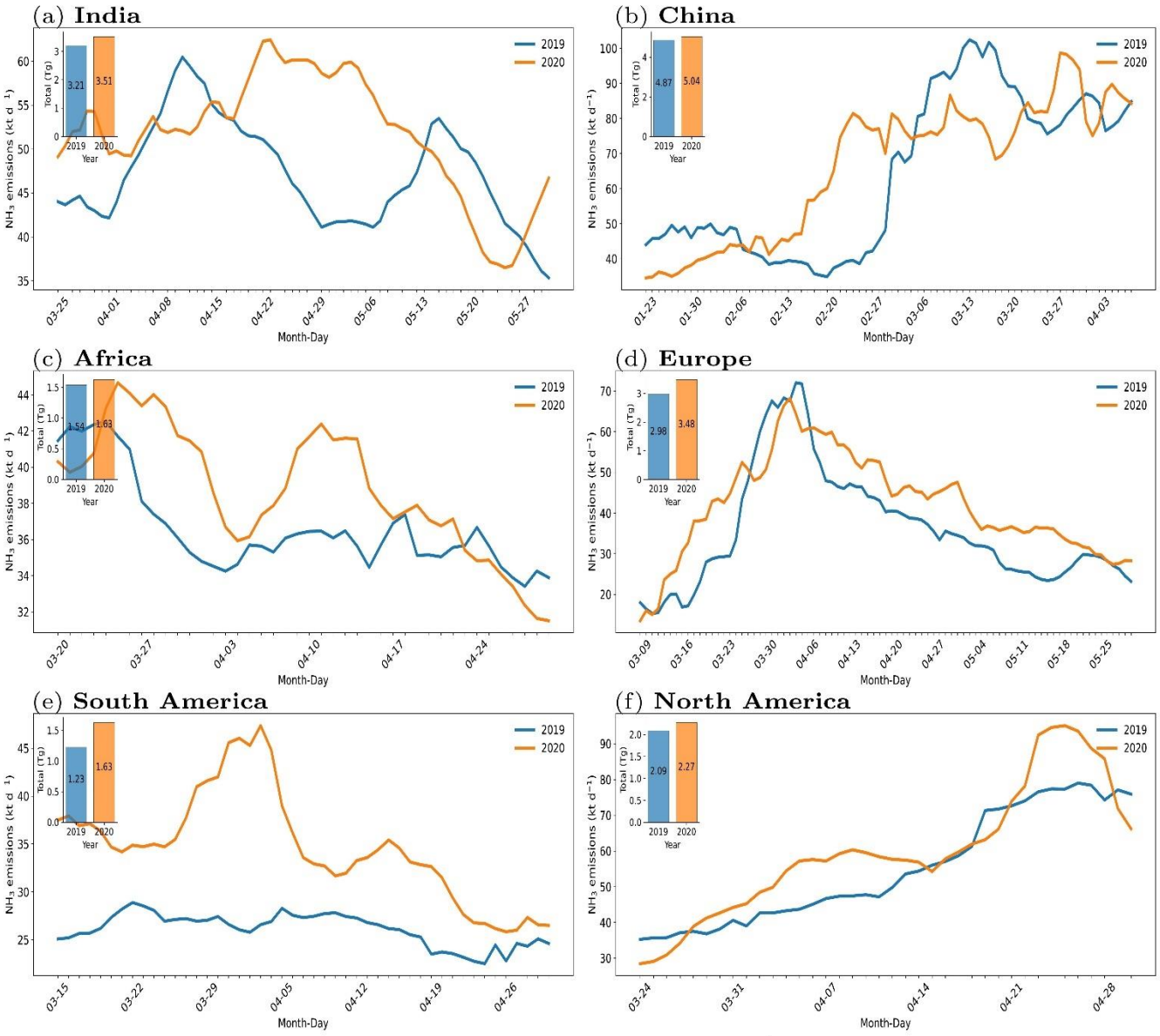
(a) India
(b) China
(c) Africa
(d) Europe
(e) South America
(f) North America
2019
2020
Month-Day
Year
Total (Tg)
3.21
3.51
4.87
5.04
1.54
1.63
2.98
3.48
1.23
1.63
2.09
2.27

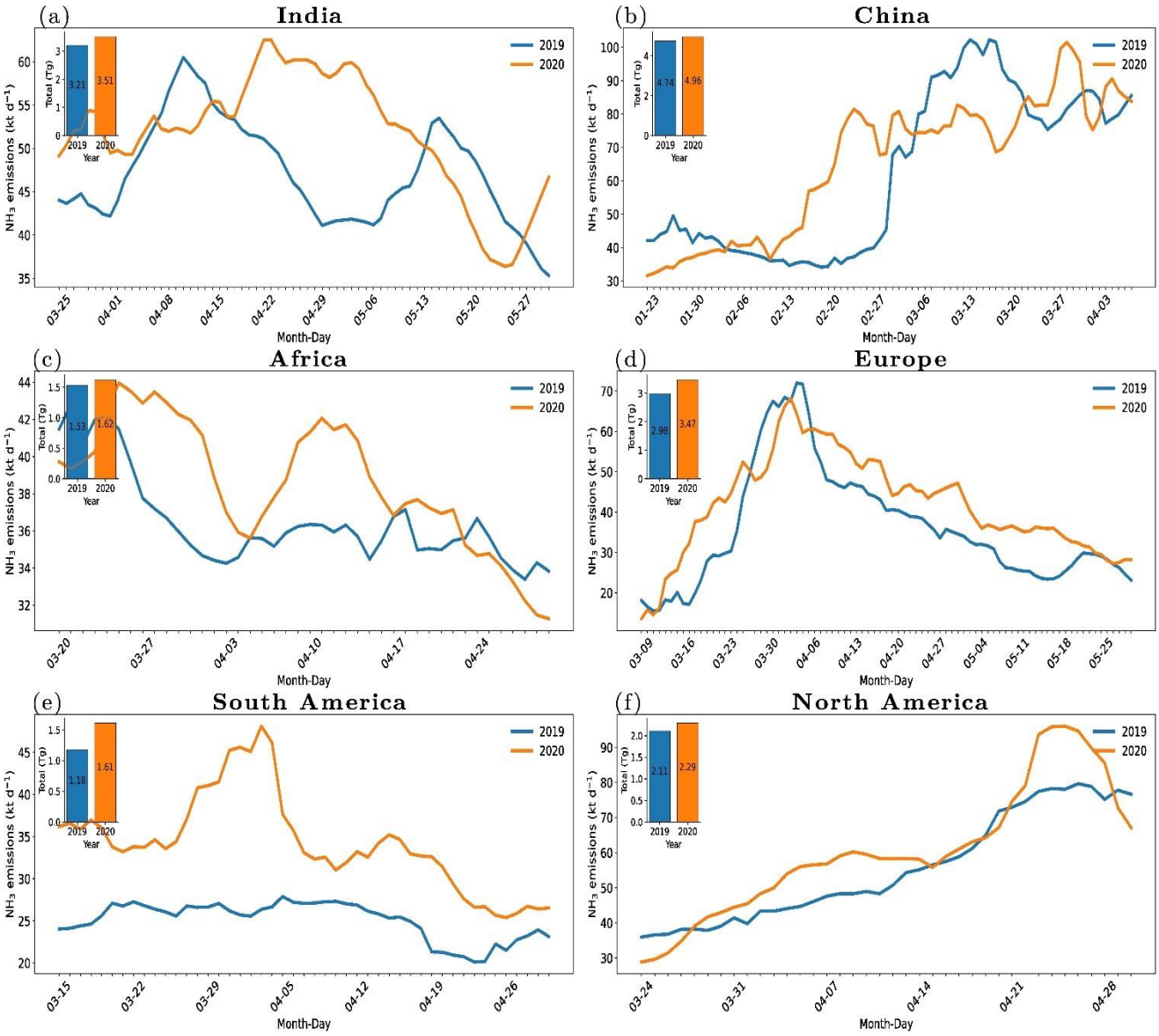

865 **Figure~~s~~ 10~~9~~:** The timeseries of estimated daily (at 10-day scale) NH_3 emissions and total emissions (bar plots) during the COVID-19 lockdown periods in the year 2020 and pre-COVID year 2019 over different regions across the world.

From our atmospheric inversions, we observe that the annual NH_3 emissions worldwide and across all the selected six regions in the COVID-19 lockdowns year 2020 are higher compared to the pre-COVID year 2019 (Figure 6&~~8~~9). Lockdown periods varied across different regions, countries, and cities. However, following the first lockdown in China in the second last week 870 of January 2020, ~~the~~ majority of the first major lockdowns worldwide were implemented between March and May during that year. We defined the lockdown periods in 2020 using the most consistent common dates that aligned with the major lockdowns in each region. Figure ~~9~~10 compares the estimated daily NH_3 emissions timeseries and total NH_3 emissions during the COVID-19 lockdown periods in 2020 with the estimated NH_3 emissions during the corresponding period in pre-COVID year 2019 across six regions. Daily (at 10-day scale) variation of the NH_3 emission during the lockdown periods in 2020 are mostly 875 higher compared to those in same period in 2019 (Figure ~~9~~10). The total NH_3 emissions across these regions in 2020 during the lockdown periods increased by a minimum ~5~~4~~% (in China) to a maximum ~37~~3~~% (in South America) compared to the total emissions in this period in 2019 (Figure ~~9~~10). The total NH_3 emissions during the lockdown periods in 2020 compared to 2019 across India, Africa, North America, and Europe regions increase by ~10%, ~6%, ~9%, and ~16~~7~~%, respectively.

The increase in NH_3 emissions from our global inversions during the COVID-19 lockdown periods in 2020 across different 880 regions, compared to the pre-COVID year 2019, raises uncertainty about whether this rise is due to an increase in NH_3 emission sources or due to the impact of meteorology on NH_3 volatilization or due to decrease in the atmospheric sink of NH_3 due to

decline in NOx and SO_2 emissions and concentrations during the lockdowns. However, an increase in NH_3 emission sources during such these short lockdowns period seems unlikely, as agricultural practices, the primary source of NH_3 emissions, remained largely unchanged during the lockdowns. This suggests that the observed rise may be more attributable to changes in atmospheric chemistry or to the impact of meteorology on NH_3 volatilization and to the reduction of other species, like SO2 and NOx emissions, during the lockdowns (Evangeliou et al., 2024). The single species inversion system used in this study has a limitation and a source of uncertainty to explain this rise in NH_3 emissions. These changes require to study the atmospheric chemistry of ammonia in response to variations in NOx and SO_2 levels in the atmosphere. A combined multi-species inversion of NOx, SO_2, and NH_3 emissions would offer valuable insights into the complex chemical interactions among these air pollutant species in the atmosphere.

4.3 Uncertainties and ~~L~~limitations of the present study

There are several uncertainties and limitations associated with our global daily (at 10-day scale) inversion of the anthropogenic NH_3 emissions using IASI NH_3 observations. Although our estimates are mostly consistent and within the range of other recent inversion emissions, our inversion approach and estimates ~~is~~ are subject to several uncertainties and limitations. The inversion approach is directly impacted by the errors associated with the observations from the satellite NH_3 retrievals, and from model simulations and it does not provide the uncertainty in emission estimates. A few studies (Cooper et al., 2017; Koukouli et al., 2018) provided some information about the uncertainties in their estimates of other short-lived species like NOx or SO_2 using basic or FDMB inversion approach, propagating the observation errors. Although, their estimates of uncertainties do not provide the full uncertainty budget as they do not account for uncertainties associated with model errors or the specific modeling approach, an implementing of a similar approach could be considered in future to provide some indication of the uncertainties in our inversion estimates. Systematic errors in satellite retrievals, particularly notable at higher latitudes and during wintertime, may introduce inconsistencies or lead to an overestimation of emissions. Statistical inverse modelling methods (Cao et al., 2020, 2022) account for retrieval errors, but this account is generally focused on the random local and instant noise on the retrievals, and these methods are also highly impacted by systematic errors (Cao et al., 2020, 2022).

The FDMB inversion approach employs a linear sensitivity function based on the perturbations of NH_3 emissions in LMDZ-INCA model simulations, which may oversimplify the complex chemical interactions between air pollutants, including NH_3, in the atmosphere. However, in order to test the impact on the inversion results of the selection of the level of perturbations, we have also conducted a sensitivity analysis with a LMDZ-INCA model simulation using a smaller 20% perturbation to the prior CEDS anthropogenic NH_3 emissions for the year 2019, in contrast to the original 40% perturbation used in our FDMB inversion setup. The results show that the differences in the resulting budget of the estimated NH_3 emissions over 2019 and the globe with the application of the FDMB based on these two levels of perturbations are less than 2%, indicating that the inversion results are not highly sensitive to the choice of perturbation magnitude within this range. The good fit between the model simulations with the inverted NH_3 emissions and the IASI NH_3 observations (section 3.2) further strengthens the confidence in the linearization of the inversion problem based on 40% perturbations to the prior estimate of the emissions. This sensitivity behavior is similar with that from previous applications of the FDMB method to the inversions of anthropogenic NOx emissions, where different perturbation levels (e.g., 5-50%) to the prior emissions resulted in minimal changes in the posterior anthropogenic NOx emission estimates at global and regional scales (Cooper et al., 2017; Lamsal et al., 2011; Zheng et al., 2020). The use of a 40% perturbation in our NH_3 study was motivated by the relatively high uncertainty in current NH_3 emission inventories, particularly over regions with strong agricultural sources. Nevertheless, our sensitivity test indicates that this choice (at least within a range of 20-40%) is not a critical parameter of our inversions.

~~-~~Due to the sparseness of daily satellite observations of NH_3 total columns, when the number of high-quality observations within a grid cell are limited, it amplifies uncertainty in the averaged gridded dataset used in the inversions. Consequently, this may lead to an increase in uncertainty in the estimates of daily (at 10-day scale) emissions. As we focus on the inversion of

dominated anthropogenic NH_3 emissions, exclusion of the emissions from other sectors like natural sources is a big challenge. This complexity is particularly pronounced in the regions dominated by biomass-burning NH_3 emissions from wildfires. The local mass-balance inversion approach does not incorporate the transport of ammonia from the non-local biomass-burning emissions regions to the local anthropogenic grids, which may lead to an overestimation of the anthropogenic NH_3 emissions in some regions like South America, North America, and Africa. Furthermore, the conservative gap-filling approach employed in this study may introduce some biases and contribute to uncertainties in the final emission estimates.

Although, the local finite difference mass-balance approach applied for the inversion of short-lived species like NH_3 in this study, which has a typical ~~very~~ short atmospheric lifetime of a few hours to a day, is suitable for inversions at a coarse resolution (~2°) (Cooper et al., 2017),~~.~~ our model's spatial resolution's (1.27° × 2.5°) typical length scale can often be reached by the advection of NH_3 within its lifetime. The transport to neighboring grids can lead to a spatial "smearing" effect, where emissions are dispersed away from their source grid cell, introducing errors in mass balance inversion approaches (Cooper et al., 2017; Li et al., 2019). This problem of spatial smearing in mass balance inversion approaches is well-documented for short-lived species like NOx or NH_3 (Cooper et al., 2017; Li et al., 2019). Such smearing can lead, on average, to the under-estimation of the regional scale emissions, since the approach overlook the fact that the amplitude of the NH_3 signal associated to a given area source decreases with the advection downwind (Cooper et al., 2017; Li et al., 2019). For short-lived species like NOx, some approaches such as smoothing kernels or iterative FDMB inversion approaches have been used to reduce these errors, but the latter is computationally intensive, especially for global inversions. An iterative ~~finite difference mass balance~~FDMB approach (Cooper et al., 2017; Li et al., 2019) can be explored in future to provide a better accuracy in the estimates of NH_3 emissions at a feasible computational cost to overcome this limitation.

In our LMDZ-INCA model setup and inversion framework, the CEDS inventory emissions are re-gridded to match the model resolution. While this inevitably misses some fine-scale features, our study focuses on the broader regional patterns of NH_3 emissions rather than point-source inversions. The inversions at higher resolution, based on high-resolution regional inventories (e.g., MEIC, NEI, CAMS-REG, etc.) and high-resolution chemistry transport model simulations can bring more robust information of the more localized NH_3 sources such as point sources at sub-national scales. However, the above-mentioned limitation, spatial spearing effect (ignoring the advection across the chemistry transport model grid cells) of the FDMB inversion approach would be exacerbated at such a higher resolution. Even using iterative FDMB approach to overcome this smearing effect at finer resolutions, errors in the derived emission estimates can be amplified (Li et al., 2019). Therefore, application of such an inversion approach at the finer resolution may have limitations to accurately estimate the NH_3 emissions.

Note that, an inverse modelling framework including observations of the full reduced nitrogen family (NHx = NH_3 + NH4+) and relying on tests of sensitivities of NH_3 and NH4+ to changes in NH_3 emissions could provide a more comprehensive constraint on NH_3 emissions, given the rapid gas-particle partitioning of NH_3 to NH4+ under typical atmospheric conditions. However, current satellite retrievals such as those from IASI and CrIS are primarily focused on gaseous NH_3. The current spaceborne instruments have a limited capability to detect particulate-phase NH4+. As a result, the observational constraints in our inversion framework are based only on NH_3 columns. Nevertheless, the LMDZ-INCA aerosols-chemistry transport model used in our inversion framework fully represents these chemical conversions of NH_3 to NH4+ and the partitioning and deposition processes affecting the entire NHx family. Therefore, the LMDZ-INCA model and, implicitly, our inversion framework account for the fate of NH_3 through its interaction with NH4+ when deriving relationships between the NH_3 emissions and concentrations.

Over some regions like China and India, the rapid changes in SO_2 emissions in the recent years impact the NH_3 concentration in the atmosphere significantly and thus emissions (Luo et al., 2022). Similarly change in NOx emissions and concentration in the atmosphere across different regions alter the formation of ammonium nitrate from ambient ammonia. Therefore, we will

965 investigate the potential of simultaneously assimilating NH_3, SO_2, and NOx satellite observations to constrain the NH_3 emissions in future studies.

5 Conclusions

In this study, we present satellite-based atmospheric inversion estimates of the global daily (at 10-day scale) NH_3 emissions for a period of four years from 2019 to 2022 at 1.27°×2.5° horizontal resolution using the new version 4 of the IASI ANNI-
970 NH3-v4 NH_3 observations and the LMDZ-INCA model simulations. We take advantage of the averaging kernel provided in the IASI ANNI-NH3-v4 data product to evaluate the LMDZ-INCA model suitability for global inversion of the NH_3 emissions. The LMDZ-INCA model simulated NH_3 total columns using the prior NH_3 emissions are underestimated from the IASI NH_3 observations over most of the selected regions, except over the Indian region, and over a region in Eastern Siberia, where model shows an overall overestimation from the observations. The simulated NH_3 columns from the LMDZ-INCA model
975 followed the seasonality of the IASI observations over the South American and North American regions, and to some extent, over the European region. However, the seasonal variations over the Indian, Chinese, and African regions are inadequately represented in the model simulations compared to the IASI observations.

We use a simple finite difference mass-balance approach for the inversion of global daily (at 10-day scale) NH_3 emissions using the LMDZ-INCA and IASI NH_3 total NH_3 columns which uses a sensitivity parameter of NH_3 columns to changes in
980 the local NH_3 emissions to address non-linear chemistry affects from the model simulations. By conducting an evaluation simulation with the LMDZ-INCA model using IASI-constrained NH_3 emission estimates derived from our global atmospheric inversions for the year 2019, we demonstrate that the substantial improvements in model agreement with the IASI NH_3 observations compared to those using prior NH_3 emissions, across different spatiotemporal scale, strongly validate the robustness and internal consistency of our inversion framework, despite its simplified linearization approach. Our inversions
985 provided an average of ~978 (~~95~~94–~~101~~100) Tg yr^{-1} global annual NH_3 emission over a period of four years from 2019 to 2022. Our IASI-constrained NH_3 emission estimates are ~613% (~557%-658%) higher than the prior CEDS anthropogenic NH_3 emissions used in the inversions. A comparison of our inversion estimates with the two independent global bottom-up inventories CAMS and CAMEO shows that our estimates are ~1.8~~9~~ times higher than CAMS anthropogenic NH_3 emissions and ~1.4 times higher than CAMEO's combined agricultural and natural soil NH_3 emissions. Our global and regional NH_3
990 emission estimates over India, China, Africa, Europe, South America, North America, and the Middle East regions are mostly within the range of other global and regional inversion estimates derived based on the IASI or CrIS satellite NH_3 observations. Our simple inversion framework lacks the ability to attribute contributions from the sectors like the biomass burning on the estimates of the anthropogenic NH_3 emissions. Therefore, the estimated NH_3 emissions over some regions like South America and Africa regions may be overestimated due to dominating biomass burning from wildfires in these regions. Our NH_3 emission
995 estimates over the Europe are ~728% higher compared to the prior CEDS inventory emissions; however, they are consistent with two recent inversion estimates. We observed an increasing trend of the NH_3 emission over the China and Africa, and a decreasing trend over the Indian region over a four-year period from 2019 to 2022. Our estimates of the NH_3 emissions show a strong seasonal variation over most of the selected regions which are currently poorly known or almost absent in bottom-up inventories.

1000 We also analyzed impact of restrictions during COVID-19 lockdown periods in 2020 over different regions across the world on the estimated daily (at 10-day scale) NH_3 emissions in comparison to the pre-COVID year 2019. Our inversion estimates show that the total NH_3 emissions across China, India, Africa, North America, Europe, and South American regions during the lockdown periods in the year 2020 increased by respectively ~54%, ~10%, ~6%, ~9%, ~167%, and ~373% compared to the total emissions in the same periods in 2019. However, this increase in NH_3 emissions from our global atmospheric
1005 inversions during the COVID-19 lockdowns, compared to the pre-COVID year 2019, raises a question about whether this rise is due to an increase in NH_3 emission sources or due to the impact of meteorology on NH_3 volatilization or due to decrease in

the atmospheric sink of atmospheric NH_3 due to decline in NOx and SO_2 emissions and ambient concentrations during the lockdown periods. However, our inversion system fails to explain this rise in NH_3 emissions. Therefore, a more comprehensive inversion approach, integrating NOx, SO_2, and NH_3 simultaneously, would provide deeper insights into the complex chemical interactions between these pollutants in the atmosphere.

Code and data availability

All the estimated emission dataset will be available from the ESA World Emission (WOREM) project website (https://www.world-emission.com). The IASI-ANNI-NH3 version 4 dataset is available from the Aeris data infrastructure https://iasi.aeris-data.fr/nh3/. CAMS anthropogenic emissions CAMS-GLOB-ANT_v5.3 data can be accessed directly from https://eccad.aeris-data.fr/essd-surf-emis-cams-ant/. The NH_3 emission estimates from dataset Luo et al. (2022) for the year 2018, used for comparison analysis, are available from GitHub: https://github.com/bnulzq/NH3-emission.git. The codes and scripts developed for inversions, plotting, and other analysis are accessible upon reasonable request from the corresponding author. The version of the LMDZ-INCA model used in this study is available from https://forge.ipsl.jussieu.fr/igcmg/svn/modipsl/trunk.

Author contribution

PK: Conceptualization, computations, codes development, data curation, formal analysis, investigation, methodology, validation, visualization, writing (original draft), review and editing. **GB, DH, PCi:** Conceptualization, supervision, methodology, investigation, funding acquisition, project administration, writing, review and editing. **MB:** CAMEO inventory NH3 emission dataset, review and editing. **LC, MVM, PCo:** IASI version 4 NH3 dataset, review and editing. **AC:** LMDZ-INCA model, review and editing. **BZ:** CEDS inventory emission dataset, review and editing. **BRR:** Project administration, Funding acquisition, review and editing. **AD:** Project administration, Funding acquisition, review and editing.

Competing interests

The contact author has declared that none of the authors has any competing interests.

Acknowledgements

This study received funding from the ESA WORld EMission (WOREM) project (https://www.world-emission.com) (ESA Contract No. 4000137291/22/I-EF). DH also acknowledges the support from the Research Council of Norway under project No. 336227 "AMMONIA: Climate and environmental impacts of green ammonia (NH3)". The simulations were performed using HPC resources from GENCI (Grand Equipement National de Calcul Intensif) under project gen2201. We extend our gratitude to all the data providers whose contributions were essential to this study. We wish to thank Julien Bruna (LSCE) and his team for computer support. L.C. is a Senior Research Associate supported by the Belgian F.R.S.-FNRS. MVD is supported by the FED-tWIN project ARENBERG ("Assessing the Reactive Nitrogen Budget and Emissions at Regional and Global Scales") funded via the Belgian Science Policy Office (BELSPO).

References

Beale, C. A., Paulot, F., Randles, C. A., Wang, R., Guo, X., Clarisse, L., Van Damme, M., Coheur, P. F., Clerbaux, C., Shephard, M. W., Dammers, E., Cady-Pereira, K., and Zondlo, M. A.: Large sub-regional differences of ammonia seasonal patterns over India reveal inventory discrepancies, Environmental Research Letters, 17, 104006, https://doi.org/10.1088/1748-9326/AC881F, 2022.

Beaudor, M., Vuichard, N., Lathiere, J., Evangeliou, N., Van Damme, M., Clarisse, L., and Hauglustaine, D.: Global agricultural ammonia emissions simulated with the ORCHIDEE land surface model, Geosci Model Dev, 16, 1053–1081, https://doi.org/10.5194/GMD-16-1053-2023, 2023.

Beaudor, M., Vuichard, N., Lathière, J., and Hauglustaine, D.: Future trends of global agricultural emissions of ammonia in a changing climate, https://doi.org/10.22541/essoar.170542263.35872590/v1, 16 January 2024.

Beer, R., Shephard, M. W., Kulawik, S. S., Clough, S. A., Eldering, A., Bowman, K. W., Sander, S. P., Fisher, B. M., Payne, V. H., Luo, M., Osterman, G. B., and Worden, J. R.: First satellite observations of lower tropospheric ammonia and methanol, Geophys Res Lett, 35, https://doi.org/10.1029/2008GL033642, 2008.

Behera, S. N., Sharma, M., Aneja, V. P., and Balasubramanian, R.: Ammonia in the atmosphere: A review on emission sources, atmospheric chemistry and deposition on terrestrial bodies, Environmental Science and Pollution Research, 20, 8092–8131, https://doi.org/10.1007/S11356-013-2051-9/METRICS, 2013a.

Behera, S. N., Sharma, M., Aneja, V. P., and Balasubramanian, R.: Ammonia in the atmosphere: A review on emission sources, atmospheric chemistry and deposition on terrestrial bodies, Environmental Science and Pollution Research, 20, 8092–8131, https://doi.org/10.1007/S11356-013-2051-9/METRICS, 2013b.

Boersma, K. F., Eskes, H. J., and Brinksma, E. J.: Error analysis for tropospheric NO2 retrieval from space, Journal of Geophysical Research: Atmospheres, 109, 4311, https://doi.org/10.1029/2003JD003962, 2004.

Boucher, O., Servonnat, J., Albright, A. L., Aumont, O., Balkanski, Y., Bastrikov, V., Bekki, S., Bonnet, R., Bony, S., Bopp, L., Braconnot, P., Brockmann, P., Cadule, P., Caubel, A., Cheruy, F., Codron, F., Cozic, A., Cugnet, D., D'Andrea, F., Davini, P., de Lavergne, C., Denvil, S., Deshayes, J., Devilliers, M., Ducharne, A., Dufresne, J. L., Dupont, E., Éthé, C., Fairhead, L., Falletti, L., Flavoni, S., Foujols, M. A., Gardoll, S., Gastineau, G., Ghattas, J., Grandpeix, J. Y., Guenet, B., Guez, L. E., Guilyardi, E., Guimberteau, M., Hauglustaine, D., Hourdin, F., Idelkadi, A., Joussaume, S., Kageyama, M., Khodri, M., Krinner, G., Lebas, N., Levavasseur, G., Lévy, C., Li, L., Lott, F., Lurton, T., Luyssaert, S., Madec, G., Madeleine, J. B., Maignan, F., Marchand, M., Marti, O., Mellul, L., Meurdesoif, Y., Mignot, J., Musat, I., Ottlé, C., Peylin, P., Planton, Y., Polcher, J., Rio, C., Rochetin, N., Rousset, C., Sepulchre, P., Sima, A., Swingedouw, D., Thiéblemont, R., Traore, A. K., Vancoppenolle, M., Vial, J., Vialard, J., Viovy, N., and Vuichard, N.: Presentation and Evaluation of the IPSL-CM6A-LR Climate Model, J Adv Model Earth Syst, 12, e2019MS002010, https://doi.org/10.1029/2019MS002010, 2020.

Bouwman, A. F., Lee, D. S., Asman, W. A. H., Dentener, F. J., Van Der Hoek, K. W., and Olivier, J. G. J.: A global high-resolution emission inventory for ammonia, Global Biogeochem Cycles, 11, 561–587, https://doi.org/10.1029/97GB02266, 1997.

Cady-Pereira, K. E., Guo, X., Wang, R., Leytem, A. B., Calkins, C., Berry, E., Sun, K., Müller, M., Wisthaler, A., Payne, V. H., Shephard, M. W., Zondlo, M. A., and Kantchev, V.: Validation of MUSES NH3 observations from AIRS and CrIS against aircraft measurements from DISCOVER-AQ and a surface network in the Magic Valley, Atmos Meas Tech, 17, 15–36, https://doi.org/10.5194/AMT-17-15-2024, 2024.

Campbell, P. C., Tong, D., Saylor, R., Li, Y., Ma, S., Zhang, X., Kondragunta, S., and Li, F.: Pronounced increases in nitrogen emissions and deposition due to the historic 2020 wildfires in the western U.S., Science of The Total Environment, 839, 156130, https://doi.org/10.1016/J.SCITOTENV.2022.156130, 2022.

Cao, H., Henze, D. K., Shephard, M. W., Dammers, E., Cady-Pereira, K., Alvarado, M., Lonsdale, C., Luo, G., Yu, F., Zhu, L., Danielson, C. G., and Edgerton, E. S.: Inverse modeling of NH3 sources using CrIS remote sensing measurements, Environmental Research Letters, 15, 104082, https://doi.org/10.1088/1748-9326/ABB5CC, 2020.

Cao, H., Henze, D. K., Zhu, L., Shephard, M. W., Cady-Pereira, K., Dammers, E., Sitwell, M., Heath, N., Lonsdale, C., Bash, J. O., Miyazaki, K., Flechard, C., Fauvel, Y., Kruit, R. W., Feigenspan, S., Brümmer, C., Schrader, F., Twigg, M. M., Leeson, S., Tang, Y. S., Stephens, A. C. M., Braban, C., Vincent, K., Meier, M., Seitler, E., Geels, C., Ellermann, T., Sanocka, A., and Capps, S. L.: 4D-Var Inversion of European NH3 Emissions Using CrIS NH3 Measurements and GEOS-Chem Adjoint With Bi-Directional and Uni-Directional Flux Schemes, Journal of Geophysical Research: Atmospheres, 127, e2021JD035687, https://doi.org/10.1029/2021JD035687, 2022.

Chen, J., Cheng, M., Krol, M., de Vries, W., Zhu, Q., Liu, X., Zhang, F., and Xu, W.: Trends in anthropogenic ammonia emissions in China since 1980: A review of approaches and estimations, Front Environ Sci, 11, 1133753, https://doi.org/10.3389/FENVS.2023.1133753/BIBTEX, 2023a.

Chen, Y., Shen, H., Kaiser, J., Hu, Y., Capps, S. L., Zhao, S., Hakami, A., Shih, J. S., Pavur, G. K., Turner, M. D., Henze, D. K., Resler, J., Nenes, A., Napelenok, S. L., Bash, J. O., Fahey, K. M., Carmichael, G. R., Chai, T., Clarisse, L., Coheur, P. F., Van Damme, M., and Russell, A. G.: High-resolution hybrid inversion of IASI ammonia columns to constrain US ammonia emissions using the CMAQ adjoint model, Atmos Chem Phys, 21, 2067–2082, https://doi.org/10.5194/ACP-21-2067-2021, 2021.

Chen, Y., Hall, J., van Wees, D., Andela, N., Hantson, S., Giglio, L., van der Werf, G. R., Morton, D. C., and Randerson, J. T.: Multi-decadal trends and variability in burned area from the 5th version of the Global Fire Emissions Database (GFED5), https://doi.org/10.5194/essd-2023-182, 26 May 2023b.

Clarisse, L., Clerbaux, C., Dentener, F., Hurtmans, D., and Coheur, P. F.: Global ammonia distribution derived from infrared satellite observations, Nat Geosci, 2, 479–483, https://doi.org/10.1038/NGEO551, 2009.

Clarisse, L., Shephard, M. W., Dentener, F., Hurtmans, D., Cady-Pereira, K., Karagulian, F., Van Damme, M., Clerbaux, C., and Coheur, P. F.: Satellite monitoring of ammonia: A case study of the San Joaquin Valley, Journal of Geophysical Research: Atmospheres, 115, 13302, https://doi.org/10.1029/2009JD013291, 2010.

Clarisse, L., Franco, B., Van Damme, M., Di Gioacchino, T., Hadji-Lazaro, J., Whitburn, S., Noppen, L., Hurtmans, D., Clerbaux, C., and Coheur, P.: The IASI NH_3 version 4 product: averaging kernels and improved consistency, Atmos Meas Tech, 16, 5009–5028, https://doi.org/10.5194/amt-16-5009-2023, 2023.

Clerbaux, C., Boynard, A., Clarisse, L., George, M., Hadji-Lazaro, J., Herbin, H., Hurtmans, D., Pommier, M., Razavi, A., Turquety, S., Wespes, C., and Coheur, P. F.: Monitoring of atmospheric composition using the thermal infrared IASI/MetOp sounder, Atmos Chem Phys, 9, 6041–6054, https://doi.org/10.5194/ACP-9-6041-2009, 2009.

Cooper, M., Martin, R. V., Padmanabhan, A., and Henze, D. K.: Comparing mass balance and adjoint methods for inverse modeling of nitrogen dioxide columns for global nitrogen oxide emissions, Journal of Geophysical Research: Atmospheres, 122, 4718–4734, https://doi.org/10.1002/2016JD025985, 2017.

Cooper, M. J., Martin, R. V., Henze, D. K., and Jones, D. B. A.: Effects of a priori profile shape assumptions on comparisons between satellite NO2 columns and model simulations, Atmos Chem Phys, 20, 7231–7241, https://doi.org/10.5194/ACP-20-7231-2020, 2020.

Crippa, M., Guizzardi, D., Muntean, M., Schaaf, E., Dentener, F., Van Aardenne, J. A., Monni, S., Doering, U., Olivier, J. G. J., Pagliari, V., and Janssens-Maenhout, G.: Gridded emissions of air pollutants for the period 1970-2012 within EDGAR v4.3.2, Earth Syst Sci Data, 10, 1987–2013, https://doi.org/10.5194/ESSD-10-1987-2018, 2018.

Van Damme, M., Whitburn, S., Clarisse, L., Clerbaux, C., Hurtmans, D., and Coheur, P. F.: Version 2 of the IASI NH3 neural network retrieval algorithm: Near-real-time and reanalysed datasets, Atmos Meas Tech, 10, 4905–4914, https://doi.org/10.5194/AMT-10-4905-2017, 2017.

Van Damme, M., Clarisse, L., Whitburn, S., Hadji-Lazaro, J., Hurtmans, D., Clerbaux, C., and Coheur, P. F.: Industrial and agricultural ammonia point sources exposed, Nature 2018 564:7734, 564, 99–103, https://doi.org/10.1038/s41586-018-0747-1, 2018.

Van Damme, M., Clarisse, L., Franco, B., Sutton, M. A., Erisman, J. W., Wichink Kruit, R., Van Zanten, M., Whitburn, S., Hadji-Lazaro, J., Hurtmans, D., Clerbaux, C., and Coheur, P. F. ois: Global, regional and national trends of atmospheric ammonia derived from a decadal (2008–2018) satellite record, Environmental Research Letters, 16, 055017, https://doi.org/10.1088/1748-9326/ABD5E0, 2021.

Dammers, E., McLinden, C. A., Griffin, D., Shephard, M. W., Van Der Graaf, S., Lutsch, E., Schaap, M., Gainairu-Matz, Y., Fioletov, V., Van Damme, M., Whitburn, S., Clarisse, L., Cady-Pereira, K., Clerbaux, C., Francois Coheur, P., and Erisman,

J. W.: NH3 emissions from large point sources derived from CrIS and IASI satellite observations, Atmos Chem Phys, 19, 12261–12293, https://doi.org/10.5194/ACP-19-12261-2019, 2019.

Dammers, E., Shephard, M., Chow, E., White, E., Hickman, J., Tokaya, J., Lutsch, E., Kharol, S., van der Graaf, S., Cady-Pereira, K., Bittman, S., McLinden, C., Erisman, J. W., and Schaap, M.: County-level ammonia emissions monitored worldwide, https://doi.org/10.21203/RS.3.RS-1752718/V1, 2022.

Ding, J., van der A, R. J., Eskes, H. J., Mijling, B., Stavrakou, T., van Geffen, J. H. G. M., and Veefkind, J. P.: NOx Emissions Reduction and Rebound in China Due to the COVID-19 Crisis, Geophys Res Lett, 47, e2020GL089912, https://doi.org/10.1029/2020GL089912, 2020.

Ding, J., van der A, R., Eskes, H., Dammers, E., Shephard, M., Wichink Kruit, R., Guevara, M., and Tarrason, L.: Ammonia emission estimates using CrIS satellite observations over Europe, Atmos Chem Phys, 24, 10583–10599, https://doi.org/10.5194/acp-24-10583-2024, 2024.

Douros, J., Eskes, H., van Geffen, J., Boersma, K. F., Compernolle, S., Pinardi, G., Blechschmidt, A.-M., Peuch, V.-H., Colette, A., and Veefkind, P.: Comparing Sentinel-5P TROPOMI NO_2 column observations with the CAMS regional air quality ensemble, Geosci Model Dev, 16, 509–534, https://doi.org/10.5194/gmd-16-509-2023, 2023.

EEA Report No 4/2023: European Union emission inventory report 1990-2021 — European Environment Agency, https://doi.org/doi:10.2800/68478, 2023.

Emanuel, K. A.: A Scheme for Representing Cumulus Convection in Large-Scale Models, Journal of Atmospheric Sciences, 48, 2313–2329, https://doi.org/https://doi.org/10.1175/1520-0469(1991)048<2313:ASFRCC>2.0.CO;2, 1991.

Eskes, H. J. and Boersma, K. F.: Averaging kernels for DOAS total-column satellite retrievals, Atmos Chem Phys, 3, 1285–1291, https://doi.org/10.5194/ACP-3-1285-2003, 2003.

Evangeliou, N., Balkanski, Y., Eckhardt, S., Cozic, A., Van Damme, M., Coheur, P. F., Clarisse, L., Shephard, M. W., Cady-Pereira, K. E., and Hauglustaine, Di.: 10-year satellite-constrained fluxes of ammonia improve performance of chemistry transport models, Atmos Chem Phys, 21, 4431–4451, https://doi.org/10.5194/ACP-21-4431-2021, 2021.

Evangeliou, N., Tichy, O., Svendby Otervik, M., Eckhardt, S., Balkanski, Y., and Hauglustaine, D.: Unchanged PM2.5 levels over Europe during COVID-19 were buffered by ammonia, https://doi.org/10.5194/AR-2024-22, 2024.

Fortems-Cheiney, A., Dufour, G., Dufossé, K., Couvidat, F., Gilliot, J. M., Siour, G., Beekmann, M., Foret, G., Meleux, F., Clarisse, L., Coheur, P. F., Van Damme, M., Clerbaux, C., and Génermont, S.: Do alternative inventories converge on the spatiotemporal representation of spring ammonia emissions in France, Atmos Chem Phys, 20, 13481–13495, https://doi.org/10.5194/ACP-20-13481-2020, 2020.

Ge, Y., Vieno, M., Stevenson, D. S., Wind, P., and Heal, M. R.: A new assessment of global and regional budgets, fluxes, and lifetimes of atmospheric reactive N and S gases and aerosols, Atmos Chem Phys, 22, 8343–8368, https://doi.org/10.5194/ACP-22-8343-2022, 2022.

Di Gioacchino, T., Clarisse, L., Noppen, L., Van Damme, M., Bauduin, S., and Coheur, P.: Spatial and Temporal Variations of Thermal Contrast in the Planetary Boundary Layer, Journal of Remote Sensing (United States), 28, https://doi.org/10.34133/REMOTESENSING.0142/ASSET/B78B1A45-7E06-4DB5-9E5E-DC14B5870B5B/ASSETS/GRAPHIC/REMOTESENSING.0142.FIG.013.JPG, 2024.

Van Der Graaf, S., Dammers, E., Segers, A., Kranenburg, R., Schaap, M., Shephard, M. W., and Erisman, J. W.: Data assimilation of CrIS NH3 satellite observations for improving spatiotemporal NH3 distributions in LOTOS-EUROS, Atmos Chem Phys, 22, 951–972, https://doi.org/10.5194/ACP-22-951-2022, 2022.

Grandpeix, J. Y. and Lafore, J. P.: A Density Current Parameterization Coupled with Emanuel's Convection Scheme. Part I: The Models, J Atmos Sci, 67, 881–897, https://doi.org/10.1175/2009JAS3044.1, 2010.

Granier, C., Darras, S., Denier van der Gon, H., Doubalova, J., Elguindi, N., Galle, B., Gauss, M., Guevara, M., Jalkanen, J.-P., Kuenen, J., Liousse, C., Quack, B., Simpson, D., and Sindelarova, K.: The Copernicus Atmosphere Monitoring Service global and regional emissions (April 2019 version), https://doi.org/10.24380/d0bn-kx16, 2019.

Guo, X., Wang, R., Pan, D., Zondlo, M. A., Clarisse, L., Van Damme, M., Whitburn, S., Coheur, P. F., Clerbaux, C., Franco, B., Golston, L. M., Wendt, L., Sun, K., Tao, L., Miller, D., Mikoviny, T., Müller, M., Wisthaler, A., Tevlin, A. G., Murphy, J. G., Nowak, J. B., Roscioli, J. R., Volkamer, R., Kille, N., Neuman, J. A., Eilerman, S. J., Crawford, J. H., Yacovitch, T. I., Barrick, J. D., and Scarino, A. J.: Validation of IASI Satellite Ammonia Observations at the Pixel Scale Using In Situ Vertical Profiles, Journal of Geophysical Research: Atmospheres, 126, e2020JD033475, https://doi.org/10.1029/2020JD033475, 2021.

Hauglustaine, D. A., Hourdin, F., Jourdain, L., Filiberti, M. A., Walters, S., Lamarque, J. F., and Holland, E. A.: Interactive chemistry in the Laboratoire de Météorologie Dynamique general circulation model: Description and background tropospheric chemistry evaluation, Journal of Geophysical Research: Atmospheres, 109, https://doi.org/10.1029/2003JD003957, 2004.

Hauglustaine, D. A., Balkanski, Y., and Schulz, M.: A global model simulation of present and future nitrate aerosols and their direct radiative forcing of climate, Atmos Chem Phys, 14, 11031–11063, https://doi.org/10.5194/ACP-14-11031-2014, 2014.

Hourdin, F., Rio, C., Grandpeix, J. Y., Madeleine, J. B., Cheruy, F., Rochetin, N., Jam, A., Musat, I., Idelkadi, A., Fairhead, L., Foujols, M. A., Mellul, L., Traore, A. K., Dufresne, J. L., Boucher, O., Lefebvre, M. P., Millour, E., Vignon, E., Jouhaud, J., Diallo, F. B., Lott, F., Gastineau, G., Caubel, A., Meurdesoif, Y., and Ghattas, J.: LMDZ6A: The Atmospheric Component of the IPSL Climate Model With Improved and Better Tuned Physics, J Adv Model Earth Syst, 12, e2019MS001892, https://doi.org/10.1029/2019MS001892, 2020.

Iturbide, M., Gutiérrez, J. M., Alves, L. M., Bedia, J., Cerezo-Mota, R., Cimadevilla, E., Cofiño, A. S., Luca, A. Di, Faria, S. H., Gorodetskaya, I. V., Hauser, M., Herrera, S., Hennessy, K., Hewitt, H. T., Jones, R. G., Krakovska, S., Manzanas, R., Martínez-Castro, D., Narisma, G. T., Nurhati, I. S., Pinto, I., Seneviratne, S. I., Hurk, B. van den, and Vera, C. S.: An update of IPCC climate reference regions for subcontinental analysis of climate model data: definition and aggregated datasets, Earth Syst Sci Data, 12, 2959–2970, https://doi.org/10.5194/ESSD-12-2959-2020, 2020.

Jin, J., Fang, L., Li, B., Liao, H., Wang, Y., Han, W., Li, K., Pang, M., Wu, X., and Xiang Lin, H.: 4DEnVar-based inversion system for ammonia emission estimation in China through assimilating IASI ammonia retrievals, Environmental Research Letters, 18, 034005, https://doi.org/10.1088/1748-9326/ACB835, 2023.

Koukouli, M. E., Theys, N., Ding, J., Zyrichidou, I., Mijling, B., Balis, D., and Johannes Van Der A, R.: Updated SO2 emission estimates over China using OMI/Aura observations, Atmos Meas Tech, 11, 1817–1832, https://doi.org/10.5194/AMT-11-1817-2018, 2018.

Krinner, G., Viovy, N., de Noblet-Ducoudré, N., Ogée, J., Polcher, J., Friedlingstein, P., Ciais, P., Sitch, S., and Prentice, I. C.: A dynamic global vegetation model for studies of the coupled atmosphere-biosphere system, Global Biogeochem Cycles, 19, 1–33, https://doi.org/10.1029/2003GB002199, 2005.

Kuttippurath, J., Singh, A., Dash, S. P., Mallick, N., Clerbaux, C., Van Damme, M., Clarisse, L., Coheur, P. F., Raj, S., Abbhishek, K., and Varikoden, H.: Record high levels of atmospheric ammonia over India: Spatial and temporal analyses, Science of The Total Environment, 740, 139986, https://doi.org/10.1016/J.SCITOTENV.2020.139986, 2020.

Kuttippurath, J., Patel, V. K., Kashyap, R., Singh, A., and Clerbaux, C.: Anomalous increase in global atmospheric ammonia during COVID-19 lockdown: Need policies to curb agricultural emissions, J Clean Prod, 434, 140424, https://doi.org/10.1016/J.JCLEPRO.2023.140424, 2024.

Lamsal, L. N., Martin, R. V., Padmanabhan, A., Van Donkelaar, A., Zhang, Q., Sioris, C. E., Chance, K., Kurosu, T. P., and Newchurch, M. J.: Application of satellite observations for timely updates to global anthropogenic NOx emission inventories, Geophys Res Lett, 38, https://doi.org/10.1029/2010GL046476, 2011.

Li, C., Martin, R. V., Shephard, M. W., Cady-Pereira, K., Cooper, M. J., Kaiser, J., Lee, C. J., Zhang, L., and Henze, D. K.: Assessing the Iterative Finite Difference Mass Balance and 4D-Var Methods to Derive Ammonia Emissions Over North

America Using Synthetic Observations, Journal of Geophysical Research: Atmospheres, 124, 4222–4236, https://doi.org/10.1029/2018JD030183;SUBPAGE:STRING:FULL, 2019.

Liu, P., Ding, J., Liu, L., Xu, W., and Liu, X.: Estimation of surface ammonia concentrations and emissions in China from the polar-orbiting Infrared Atmospheric Sounding Interferometer and the FY-4A Geostationary Interferometric Infrared Sounder, Atmos Chem Phys, 22, 9099–9110, https://doi.org/10.5194/ACP-22-9099-2022, 2022.

Lovarelli, D., Fugazza, D., Costantini, M., Conti, C., Diolaiuti, G., and Guarino, M.: Comparison of ammonia air concentration before and during the spread of COVID-19 in Lombardy (Italy) using ground-based and satellite data, Atmos Environ, 259, 118534, https://doi.org/10.1016/J.ATMOSENV.2021.118534, 2021.

Luo, Z., Zhang, Y., Chen, W., Van Damme, M., Coheur, P. F., and Clarisse, L.: Estimating global ammonia (NH3) emissions based on IASI observations from 2008 to 2018, Atmos Chem Phys, 22, 10375–10388, https://doi.org/10.5194/ACP-22-10375-2022, 2022.

Makkaroon, P., Tong, D. Q., Li, Y., Hyer, E. J., Xian, P., Kondragunta, S., Campbell, P. C., Tang, Y., Baker, B. D., Cohen, M. D., Darmenov, A., Lyapustin, A., Saylor, R. D., Wang, Y., and Stajner, I.: Development and Evaluation of a North America Ensemble Wildfire Air Quality Forecast: Initial Application to the 2020 Western United States "Gigafire," Journal of Geophysical Research: Atmospheres, 128, e2022JD037298, https://doi.org/10.1029/2022JD037298, 2023.

Marais, E. A., Pandey, A. K., Van Damme, M., Clarisse, L., Coheur, P. F., Shephard, M. W., Cady-Pereira, K. E., Misselbrook, T., Zhu, L., Luo, G., and Yu, F.: UK Ammonia Emissions Estimated With Satellite Observations and GEOS-Chem, Journal of Geophysical Research: Atmospheres, 126, e2021JD035237, https://doi.org/10.1029/2021JD035237, 2021.

McDuffie, E. E., Smith, S. J., O'Rourke, P., Tibrewal, K., Venkataraman, C., Marais, E. A., Zheng, B., Crippa, M., Brauer, M., and Martin, R. V.: A global anthropogenic emission inventory of atmospheric pollutants from sector- And fuel-specific sources (1970-2017): An application of the Community Emissions Data System (CEDS), Earth Syst Sci Data, 12, 3413–3442, https://doi.org/10.5194/ESSD-12-3413-2020, 2020.

Messina, P., Lathière, J., Sindelarova, K., Vuichard, N., Granier, C., Ghattas, J., Cozic, A., and Hauglustaine, D. A.: Global biogenic volatile organic compound emissions in the ORCHIDEE and MEGAN models and sensitivity to key parameters, Atmos Chem Phys, 16, 14169–14202, https://doi.org/10.5194/ACP-16-14169-2016, 2016.

Momeni, M., Choi, Y., Yeganeh, A. K., Pouyaei, A., Jung, J., Park, J., Shephard, M. W., Dammers, E., and Cady-Pereira, K. E.: Constraining East Asia Ammonia Emissions Through Satellite Observations and Iterative Finite Difference Mass Balance (iFDMB) and Investigating its Impact on Inorganic Fine Particulate Matter, https://doi.org/10.2139/SSRN.4395242, 2023.

Osipov, S., Chowdhury, S., Crowley, J. N., Tadic, I., Drewnick, F., Borrmann, S., Eger, P., Fachinger, F., Fischer, H., Predybaylo, E., Fnais, M., Harder, H., Pikridas, M., Vouterakos, P., Pozzer, A., Sciare, J., Ukhov, A., Stenchikov, G. L., Williams, J., and Lelieveld, J.: Severe atmospheric pollution in the Middle East is attributable to anthropogenic sources, Communications Earth & Environment 2022 3:1, 3, 1–10, https://doi.org/10.1038/s43247-022-00514-6, 2022.

Pu, W., Guo, H., Ma, Z., Qiu, Y., Tang, Y., Liu, Q., Wang, F., and Sheng, J.: Aircraft measurements reveal vertical distribution of atmospheric ammonia over the North China Plain in early autumn, Environ Chem Lett, 18, 2149–2156, https://doi.org/10.1007/S10311-020-01051-4/FIGURES/4, 2020.

Rio, C. and Hourdin, F.: A Thermal Plume Model for the Convective Boundary Layer: Representation of Cumulus Clouds, J Atmos Sci, 65, 407–425, https://doi.org/https://doi.org/10.1175/2007JAS2256.1, 2008.

Sahoo, P., Sahu, S. K., Mangaraj, P., Mishra, A., Beig, G., and Gunthe, S. S.: Reporting of gridded ammonia emission and assessment of hotspots across India: A comprehensive study of 24 anthropogenic sources, J Hazard Mater, 479, 135557, https://doi.org/10.1016/J.JHAZMAT.2024.135557, 2024.

Shephard, M. W., Dammers, E., Cady-Pereira, K. E., Kharol, S. K., Thompson, J., Gainariu-Matz, Y., Zhang, J., McLinden, C. A., Kovachik, A., Moran, M., Bittman, S., Sioris, C. E., Griffin, D., Alvarado, M. J., Lonsdale, C., Savic-Jovcic, V., and

Zheng, Q.: Ammonia measurements from space with the Cross-track Infrared Sounder: characteristics and applications, Atmos Chem Phys, 20, 2277–2302, https://doi.org/10.5194/acp-20-2277-2020, 2020.

Someya, Y., Imasu, R., Shiomi, K., and Saitoh, N.: Atmospheric ammonia retrieval from the TANSO-FTS/GOSAT thermal infrared sounder, Atmos Meas Tech, 13, 309–321, https://doi.org/10.5194/AMT-13-309-2020, 2020.

Soulie, A., Granier, C., Darras, S., Zilbermann, N., Doumbia, T., Guevara, M., Jalkanen, J.-P., Keita, S., Liousse, C., Crippa, M., Guizzardi, D., Hoesly, R., and Smith, S.: Global Anthropogenic Emissions (CAMS-GLOB-ANT) for the Copernicus Atmosphere Monitoring Service Simulations of Air Quality Forecasts and Reanalyses, Earth System Science Data Discussions, 2023, 1–45, https://doi.org/10.5194/essd-2023-306, 2023.

Sutton, M. A., Reis, S., Riddick, S. N., Dragosits, U., Nemitz, E., Theobald, M. R., Tang, Y. S., Braban, C. F., Vieno, M., Dore, A. J., Mitchell, R. F., Wanless, S., Daunt, F., Fowler, D., Blackall, T. D., Milford, C., Flechard, C. R., Loubet, B., Massad, R., Cellier, P., Personne, E., Coheur, P. F., Clarisse, L., Van Damme, M., Ngadi, Y., Clerbaux, C., Skjøth, C. A., Geels, C., Hertel, O., Kruit, R. J. W., Pinder, R. W., Bash, J. O., Walker, J. T., Simpson, D., Horváth, L., Misselbrook, T. H., Bleeker, A., Dentener, F., and de Vries, W.: Towards a climate-dependent paradigm of ammonia emission and deposition, Philosophical Transactions of the Royal Society B: Biological Sciences, 368, https://doi.org/10.1098/RSTB.2013.0166, 2013.

Tichý, O., Eckhardt, S., Balkanski, Y., Hauglustaine, D., and Evangeliou, N.: Decreasing trends of ammonia emissions over Europe seen from remote sensing and inverse modelling, EGUsphere, 2023, 1–30, https://doi.org/10.5194/egusphere-2023-641, 2023.

Viatte, C., Petit, J. E., Yamanouchi, S., Van Damme, M., Doucerain, C., Germain-Piaulenne, E., Gros, V., Favez, O., Clarisse, L., Coheur, P. F., Strong, K., and Clerbaux, C.: Ammonia and PM2.5 Air Pollution in Paris during the 2020 COVID Lockdown, Atmosphere 2021, Vol. 12, Page 160, 12, 160, https://doi.org/10.3390/ATMOS12020160, 2021.

Vira, J., Hess, P., Melkonian, J., and Wieder, W. R.: An improved mechanistic model for ammonia volatilization in Earth system models: Flow of Agricultural Nitrogen version 2 (FANv2), Geosci Model Dev, 13, 4459–4490, https://doi.org/10.5194/GMD-13-4459-2020, 2020.

Wang, W., Liu, C., Clarisse, L., Van Damme, M., Coheur, P.-F., Xie, Y., Shan, C., Hu, Q., Zhang, H., Sun, Y., Yin, H., and Jones, N.: Spatial distribution and seasonal variability in atmospheric ammonia measured from ground-based FTIR observations at Hefei, China, https://doi.org/10.5194/AMT-2020-39, 2020.

Warner, J. X., Wei, Z., Larrabee Strow, L., Dickerson, R. R., and Nowak, J. B.: The global tropospheric ammonia distribution as seen in the 13-year AIRS measurement record, Atmos Chem Phys, 16, 5467–5479, https://doi.org/10.5194/ACP-16-5467-2016, 2016.

Van Der Werf, G. R., Randerson, J. T., Giglio, L., Van Leeuwen, T. T., Chen, Y., Rogers, B. M., Mu, M., Van Marle, M. J. E., Morton, D. C., Collatz, G. J., Yokelson, R. J., and Kasibhatla, P. S.: Global fire emissions estimates during 1997-2016, Earth Syst Sci Data, 9, 697–720, https://doi.org/10.5194/ESSD-9-697-2017, 2017.

Whitburn, S., Van Damme, M., Clarisse, L., Bauduin, S., Heald, C. L., Hadji-Lazaro, J., Hurtmans, D., Zondlo, M. A., Clerbaux, C., and Coheur, P. F.: A flexible and robust neural network IASI-NH3 retrieval algorithm, Journal of Geophysical Research: Atmospheres, 121, 6581–6599, https://doi.org/10.1002/2016JD024828, 2016.

Wyer, K. E., Kelleghan, D. B., Blanes-Vidal, V., Schauberger, G., and Curran, T. P.: Ammonia emissions from agriculture and their contribution to fine particulate matter: A review of implications for human health, J Environ Manage, 323, 116285, https://doi.org/10.1016/J.JENVMAN.2022.116285, 2022.

Xia, J., Zhou, Y., Fang, L., Qi, Y., Li, D., Liao, H., and Jin, J.: South Asia ammonia emission inversion through assimilating IASI observations, https://doi.org/10.5194/EGUSPHERE-2024-3938, 2025.

Xu, R., Tian, H., Pan, S., Prior, S. A., Feng, Y., Batchelor, W. D., Chen, J., and Yang, J.: Global ammonia emissions from synthetic nitrogen fertilizer applications in agricultural systems: Empirical and process-based estimates and uncertainty, Glob Chang Biol, 25, 314–326, https://doi.org/10.1111/GCB.14499, 2019.

Xu, R. T., Pan, S. F., Chen, J., Chen, G. S., Yang, J., Dangal, S. R. S., Shepard, J. P., and Tian, H. Q.: Half-Century Ammonia Emissions From Agricultural Systems in Southern Asia: Magnitude, Spatiotemporal Patterns, and Implications for Human Health, Geohealth, 2, 40–53, https://doi.org/10.1002/2017GH000098, 2018.

Xu, W., Zhao, Y., Wen, Z., Chang, Y., Pan, Y., Sun, Y., Ma, X., Sha, Z., Li, Z., Kang, J., Liu, L., Tang, A., Wang, K., Zhang, Y., Guo, Y., Zhang, L., Sheng, L., Zhang, X., Gu, B., Song, Y., Van Damme, M., Clarisse, L., Coheur, P. F., Collett, J. L., Goulding, K., Zhang, F., He, K., and Liu, X.: Increasing importance of ammonia emission abatement in PM2.5 pollution control, Sci Bull (Beijing), 67, 1745–1749, https://doi.org/10.1016/J.SCIB.2022.07.021, 2022.

Yamada, T.: Simulations of Nocturnal Drainage Flows by a $q^2 l$ Turbulence Closure Model, J Atmos Sci, 40, 91–106, https://doi.org/10.1175/1520-0469(1983)040<0091:SONDFB>2.0.CO;2, 1983.

Zheng, B., Geng, G., Ciais, P., Davis, S. J., Martin, R. V., Meng, J., Wu, N., Chevallier, F., Broquet, G., Boersma, F., van Der, R. A., Lin, J., Guan, D., Lei, Y., He, K., and Zhang, Q.: Satellite-based estimates of decline and rebound in China's CO2 emissions during COVID-19 pandemic, Sci Adv, 6, https://doi.org/10.1126/SCIADV.ABD4998/SUPPL_FILE/ABD4998_SM.PDF, 2020.

Zheng, B., Zhang, Q., Geng, G., Chen, C., Shi, Q., Cui, M., Lei, Y., and He, K.: Changes in China's anthropogenic emissions and air quality during the COVID-19 pandemic in 2020, Earth Syst Sci Data, 13, 2895–2907, https://doi.org/10.5194/ESSD-13-2895-2021, 2021.

Zhu, L., Henze, D. K., Bash, J. O., Cady-Pereira, K. E., Shephard, M. W., Luo, M., and Capps, S. L.: Sources and Impacts of Atmospheric NH3: Current Understanding and Frontiers for Modeling, Measurements, and Remote Sensing in North America, Curr Pollut Rep, 1, 95–116, https://doi.org/10.1007/S40726-015-0010-4/TABLES/1, 2015.